

1 **Mapping Permafrost Variability and Degradation Using Seismic Surface Waves,**
2 **Electrical Resistivity and Temperature Sensing: A Case Study in Arctic Alaska**

3 **Ahmad Tourei¹, Xiaohang Ji², Gabriel Fernando Rocha dos Santos³, Rafal Czarny³, Sergei**
4 **Rybakov⁴, Ziyi Wang², Matthew Hallissey², Eileen R. Martin^{1,5}, Ming Xiao², Tiejuan Zhu³,**
5 **Dmitry Nicolsky^{4,6}, Anne Jensen⁷**

6 ¹ Hydrologic Science and Engineering Program, Colorado School of Mines, Golden, CO, USA, ²
7 Department of Civil and Environmental Engineering, The Pennsylvania State University,
8 University Park, PA, USA, ³ Department of Geosciences, The Pennsylvania State University,
9 University Park, PA, USA, ⁴ Geophysical Institute, University of Alaska Fairbanks, Fairbanks,
10 AK, ⁵ Department of Geophysics and Department of Applied Math and Statistics, Colorado
11 School of Mines, Golden, CO, USA, ⁶ Laboratory for Integrated Research of the Arctic Land-
12 Shelf System, Tomsk State University, Tomsk, Russia, ⁷ Department of Anthropology, University
13 of Alaska Fairbanks, Fairbanks, AK, USA.

14 Corresponding author: Ahmad Tourei (tourei@mines.edu)

15
16 This paper is a non-peer reviewed preprint submitted to Earth ArXiv.

17 This paper has been submitted to the Journal of Geophysical Research: Earth Surface for
18 publication consideration.

19
20

21 **Abstract**

22 Subsurface processes significantly influence surface dynamics in permafrost regions,
23 necessitating multiple geophysical methods to reliably constrain permafrost characteristics. This
24 research uses multiple geophysical techniques to explore the spatial variability of permafrost in
25 undisturbed tundra and its degradation in disturbed tundra in Utqiagvik, Alaska. Here, we
26 integrate multiple quantitative techniques, including multichannel analysis of surface waves
27 (MASW), electrical resistivity tomography (ERT), and ground temperature sensing to
28 qualitatively study heterogeneity in permafrost's geophysical characteristics. MASW results
29 reveal active layer shear wave velocities (V_s) between 240 and 370 m/s, and permafrost V_s
30 between 450 and 1700 m/s, typically showing a low-high-low velocity pattern. Additionally, we
31 find an inverse relationship between in-situ V_s and ground temperature measurements. The V_s
32 profiles along with electrical resistivity profiles reveal cryostructures such as cryopeg and ice-
33 rich zones in the permafrost layer. The integrated results of MASW and ERT provide valuable
34 information for verifying ERT results for characterizing permafrost heterogeneity and
35 cryostructure. Corroboration of these geophysical observations with permafrost core samples'
36 stratigraphy and salinity measurements further validates these findings. This combination of
37 geophysical and temperature sensing methods along with permafrost core sampling confirms a
38 robust approach to assessing permafrost's spatial variability in coastal environments. Our results
39 also indicate that civil infrastructure systems such as gravel roads and pile foundations affect
40 permafrost by thickening the active layer, lowering the V_s , and reducing heterogeneity. We show
41 how the resulting V_s profiles can be used to estimate key parameters for designing buildings in
42 permafrost regions and maintaining existing infrastructure in polar regions.

43 **Plain Language Summary**

44 This study descriptively examines permafrost variability across a range of disturbed and
45 undisturbed locations in Utqiagvik, Alaska, using a variety of geophysical and temperature
46 measurement techniques, including seismic vibrations, electrical methods, and ground
47 temperature sensing. Geophysical profiles and maps were generated and used to identify
48 permafrost features such as ice-rich and ice-poor zones. The study found that seismic shear wave
49 velocity is influenced by ice content and can distinguish the active layer and permafrost. We
50 reinforced our geophysical observations with layering and salinity analyses from core samples,
51 confirming the effectiveness of our combined approach in assessing permafrost variability in
52 coastal regions. The research results regarding permafrost thickness reveal the impact of civil
53 infrastructure, finding that buildings and roads can cause permafrost to degrade.

54

55 **1 Introduction**

56 **1.1 Global Warming Impacts on Permafrost Degradation and Ground Thermal Regime**

57 Permafrost refers to any ground material below 0 °C for at least two consecutive years. It
58 is distributed across approximately 25% of the land surface in the northern hemisphere and is
59 highly sensitive to atmospheric temperature variation primarily caused by global warming
60 (Biskaborn et al., 2019; Lantuit et al., 2012). The Arctic average annual surface temperature has
61 increased by 3.1 °C from 1971 to 2019, which is three times faster than the global rate (AMAP,
62 2021; IPCC, 2021; Rantanen et al., 2022). In Utqiagvik Alaska (study area), the average annual

63 air temperature has risen over 4 °C since 1980, and recent decades have seen Arctic Alaska's
64 permafrost warm by 1-3 °C (Nicolosky et al., 2017; Thoman & Walsh, 2019). Increasing
65 temperature in the high-latitude permafrost regions leads to permafrost degradation, which
66 includes permafrost warming, active layer thickening, and thaw-related hazards such as the
67 development of taliks, ground subsidence and thermokarst in low-lying areas, mass wasting on
68 slopes, and thermal erosion and abrasion along riverbanks and coasts (Hjort et al., 2022). Global
69 warming causes contaminated and industrial sites in regions of stable permafrost to thaw, posing
70 a significant environmental threat (Langer et al., 2023). Permafrost degradation drives serious
71 changes in local geomorphology, hydrology, vegetation, wildlife dynamics, and greenhouse gas
72 emissions (Hjort et al., 2022; Streletskiy et al., 2015).

73 Permafrost research often focuses primarily on ground temperature due to its direct effect
74 on physical and biogeochemical soil processes, but permafrost is also affected by air
75 temperature, snow cover, soil moisture, vegetation cover, and soil properties (Lantuit et al.,
76 2012; Smith et al., 2022). In-situ monitoring using thermistors and thermocouples has shown that
77 permafrost temperatures are increasing, leading to thawing and degradation (Biskaborn et al.,
78 2019; Nicolosky et al., 2009; Nicolosky et al., 2017; Romanovsky et al., 2010; Shiklomanov et al.,
79 2010). Understanding the ground's thermal state in permafrost regions is crucial to model and
80 mitigate climate change impacts.

81 Understanding the spatial heterogeneity of permafrost in Arctic tundra is important for
82 studying geomorphological and ecosystem variations under climate change, as well as potential
83 engineering impacts. Permafrost structure is often complex due to fine-scale spatial
84 heterogeneity of properties such as temperature and ice content. Temperature, water saturation,
85 and ice content influence seismic wave velocities, including shear wave velocity (V_s) and
86 compressional wave velocity (V_p) (Coduto, 1999; Hjort et al., 2022; Ji et al., 2023; Liew et al.,
87 2022; Rocha dos Santos et al., 2022). Salinity is a key factor in coastal permafrost environments
88 such as Utqiagvik, Alaska. Studies by Brown (1969) and O'Sullivan (1966) reveal how salinity
89 affects permafrost's geochemistry and physical properties, such as its freezing point and stability.
90 Dafflon et al.'s research (2016, 2017) further demonstrates the impact of salinity on the
91 distribution and characteristics of shallow permafrost, highlighting its connection with vegetation
92 patterns and soil properties. Meyer et al. (2010) provide historical context, showing how
93 historical salinity variations have influenced the permafrost landscape over time. Salinity plays a
94 crucial role in key permafrost structures. Here we provide a brief overview of the active layer
95 and some of the key permafrost structures investigated in this paper, including cryopegs, ice-rich
96 zones (e.g., lenses), and thermokarst lakes. Jafarov et al. (2016) showed that the active layer
97 thickness (ALT) of undisturbed tundra (without infrastructure development and low to medium
98 water content) near Elson Lagoon in Utqiagvik, Alaska is approximately 0.2 to 0.6 m, measured
99 in August 2013. A thermokarst is formed when the thermal equilibrium shifts, allowing the
100 ground ice to thaw. Talik is a layer or body of year-round unfrozen ground (usually above 0 °C)
101 occurring in a permafrost zone due to a local anomaly in thermal, hydrological, or hydrochemical
102 conditions (e.g., underneath thermokarst lakes and rivers). Cryopegs can have temperatures
103 below 0°C, but freezing is prevented by freezing-point depression due to the dissolved-solids
104 content of the pore water (Van Everdingen, 1998). As the climate warms, the annual ground
105 temperature increases, and annual thawing deepens until a certain threshold is met, after which a
106 talik develops. Ice wedges form when water seeps into cracks in the ground during summer and
107 then freezes during winter. The distribution of ice formations and ice content within the
108 permafrost layer is highly variable (Liu et al., 2021). Previous studies confirm that the ice

109 content in the permafrost around Barrow is very high in the upper part and decreases with depth
110 (Brown et al., 1980). For the coastal plain along the Beaufort Sea from Point Barrow to the
111 Canadian border, Kanevskiy et al., 2013 reported an average total ice content (i.e., ice wedge,
112 segregated, and pore ice) of 83% and 82% for the primary surface and the drained-lakes basins,
113 respectively. This results in a landscape vulnerable to widespread subsidence and thermokarst
114 development, the magnitude of which may vary widely depending on surficial geology, ground
115 ice volume, and the extent of past thermokarst activity (Farquharson et al., 2019). The warming
116 and thawing of ice-rich permafrost pose changes in its interactions within the built environment
117 (Hjort et al., 2022).

118 Permafrost exhibits vastly variable properties between thawed and frozen states due to
119 the phase change of water, impacting its strength and bearing capacity, which can lead to
120 infrastructure failure (Hjort et al., 2022). The interaction between permafrost and civil
121 infrastructure contributes to permafrost degradation and increases construction and maintenance
122 costs (Streletskiy et al., 2012, 2015). While existing research primarily focuses on the influence
123 of degrading permafrost on infrastructure, it is crucial to consider the impact of civil
124 infrastructure on permafrost. Different foundations and architecture, such as pile foundations and
125 gravel roads, introduce thermal and physical impacts that can disturb the natural environment
126 and alter adjacent tundra ecosystems (Walker et al., 2022). As climate change continues, the
127 vulnerability of both civil infrastructure and permafrost systems grows, necessitating detailed
128 knowledge of risk exposure in current and future infrastructure areas (Hjort et al., 2022; Melvin
129 et al., 2017). Understanding the influence of civil infrastructure on degrading permafrost allows
130 for a realistic risk assessment.

131 1.2 Seismic and Geoelectrical Methods in Permafrost Regions

132 Seismic imaging is a commonly used technique for characterizing the subsurface in
133 permafrost regions (e.g., Justice & Zuba, 1986; Miller et al., 2000; Ramachandran et al., 2011),
134 because seismic wave velocities, including shear wave velocity and compressional wave
135 velocity, are sensitive to temperature, water saturation, and ice content (Coduto, 1999; Hjort et
136 al., 2022; Ji et al., 2023; Liew et al., 2022). One of the main advantages of seismic imaging in
137 permafrost regions is its ability to provide detailed information about the distribution and
138 continuity of permafrost and the nature of the underlying soils, even 3D profiles with high
139 resolution (e.g., Ramachandran et al., 2011; Schwamborn et al., 2002). This information is
140 important for various applications, such as infrastructure planning and design, resource
141 exploration, and environmental monitoring. Seismic refraction is a surface geophysics method
142 that utilizes the refraction of body waves through layered media (Scott & Markiewicz, 1990).
143 Seismic refraction has been used in several case studies of permafrost conditions and periglacial
144 environments (Harris & Cook, 1986; Ikeda, 2006; Schrott & Hoffmann, 2008). Joint inversion of
145 refraction seismic tomography (RST) and electrical resistivity tomography (ERT) has been used
146 to characterize Alpine rock glaciers and permafrost (Wagner et al., 2019). Brothers et al. (2016)
147 previously used seismic reflection data to delineate continuous subsea ice-bearing permafrost.

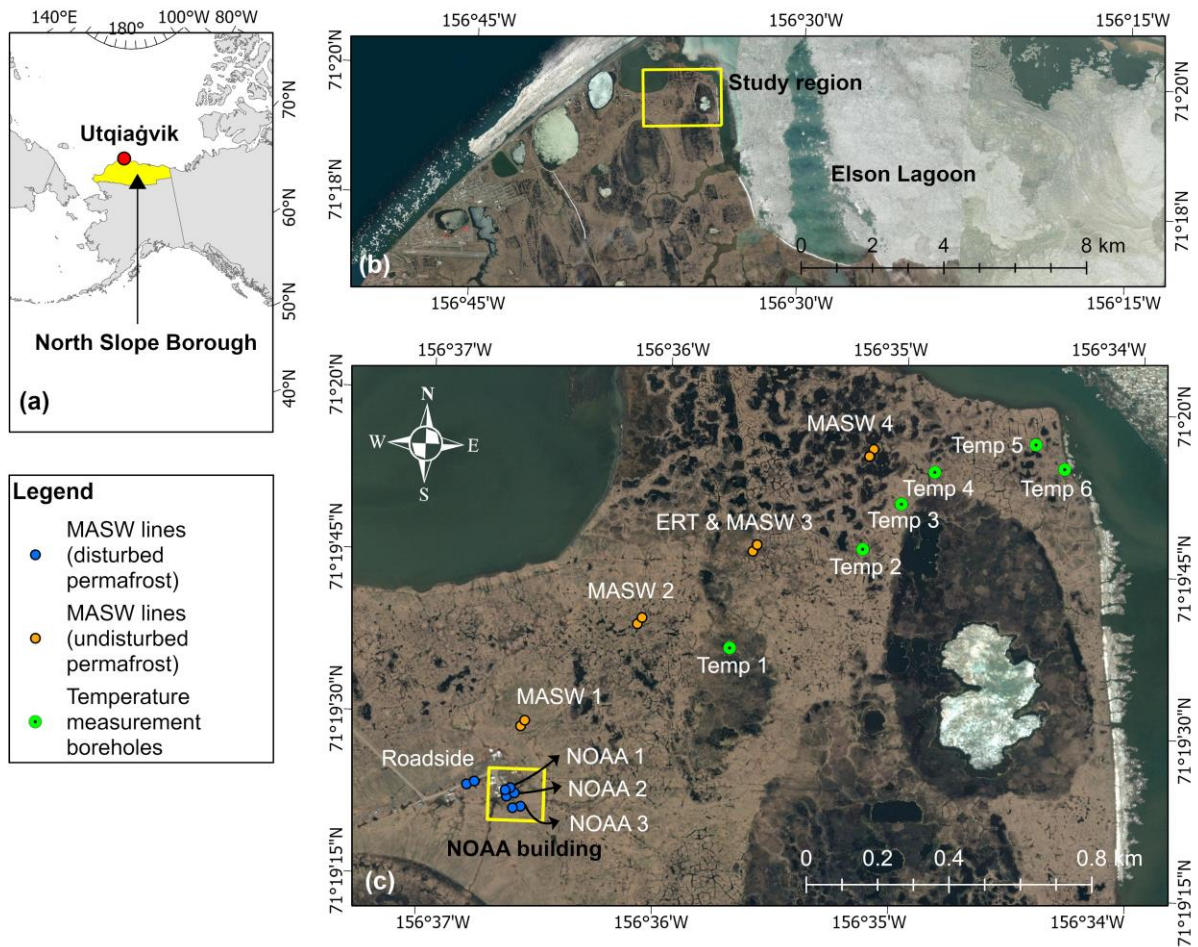
148 Surface wave methods are powerful tools for near-surface characterization of sites and
149 mapping irregular V_s profiles in permafrost through acquisition, processing, and inversion of
150 surface waves, typically Rayleigh waves (Alam & Jaiswal, 2017; Carr et al., 1998; Essien et al.,
151 2014; Fortin et al., 2007; Letson et al., 2019; Socco & Strobbia, 2004; Taylor et al., 2022).
152 Compared with seismic refraction and reflection, surface wave methods are advantageous for

153 mapping permafrost structures with low-velocity layers embedded in high-velocity permafrost
154 zones (Dou & Ajo-Franklin, 2014). Spectral Analysis of Surface Waves (SASW) has been used
155 to obtain S-wave velocity profiles of unfrozen and frozen soils in Fairbanks, Alaska (Cox et al.,
156 2012; Hazirbaba et al., 2011). Multichannel Analysis of Surface Waves (MASW) has been
157 applied in several glacial environments, including permafrost zones (Ajo-Franklin et al., 2017;
158 Dou & Ajo-Franklin, 2014; Dou et al., 2012; Glazer et al., 2020; Majdański et al., 2022; Picotti
159 et al., 2015; Rossi et al., 2018; Tourei et al., 2022). Similar to surface wave methods, ERT
160 technique excels in near-surface permafrost characterization by modeling subsurface resistivity
161 to match observed apparent resistivity data, typically yielding a two-dimensional resistivity
162 profile (Daily et al. 2000). ERT has been used in several permafrost studies to characterize
163 permafrost thaw (Etzelmüller et al., 2020), distinguish ice-content variations (Herring et al.,
164 2023), and examine interactions between permafrost and infrastructure (You et al., 2017).
165 MASW has often been combined with other technologies in permafrost research, such as seismic
166 tomography and ERT (Dou & Ajo-Franklin, 2014; Glazer et al., 2020; Marciniak et al., 2018;
167 Marciniak et al., 2019). In this study, we investigate the spatial variability of permafrost in
168 Utqiagvik, Alaska, using MASW and ERT techniques to characterize permafrost, identify
169 cryostructure, and analyze the influence of temperature on tundra permafrost systems. The
170 MASW results provide useful information to verify ERT results for subsurface features. We
171 compare in-situ temperature profiles with seismic velocity profiles to better understand the
172 ground condition of the permafrost. This study is carried out across sites in undisturbed tundra
173 and near infrastructure. Our findings underscore the impact of civil infrastructure on permafrost
174 degradation, particularly in designing and maintaining buildings in permafrost regions.

175 **2 Study Area**

176 Permafrost zones underlie 80% of Alaska, including 29% continuous permafrost
177 (Jorgenson et al., 2008). The North Slope Borough is entirely within the continuous permafrost
178 zone (Ferrians, 1965; Kerkering, 2008), shown in Figure 1a. The permafrost in Utqiagvik,
179 Alaska, is continuous and has a thickness of approximately 200–400 m (Jorgenson et al., 2008).
180 Elson Lagoon forms the eastern land boundary of the study area, shown in Figure 1b. The ALT
181 of undisturbed tundra near Elson Lagoon is approximately 0.2 to 0.6 m, and the soil volumetric
182 water content varies from 17% to 88%, measured in August 2013 (Jafarov et al., 2018). The
183 average ALT of the study area on the tundra in Utqiagvik, Alaska, is also shallow (roughly less
184 than 1.0 meter,) consisting of three distinct layers: the acrotelm (top), the catotelm (middle), and
185 the mineral soil (bottom) (Chen et al., 2020). The ground conditions vary from dry to marshy,
186 with surface vegetation. The seismic survey (MASW) operations were performed on August 6 –
187 12, 2022. The plan view showing the layout of seismic survey lines and the temperature

188 measurement locations is presented in Figure 1.



189

190 **Figure 1.** Geophysical survey and temperature measurement map: (a) Utqiagvik, North Slope
 191 Borough, Alaska. (b) Study region. (c) Seismic survey, electrical resistivity survey, and
 192 temperature measurement locations.

193

194 3 Analytical Methods

195 3.1 The MASW Technique

196 Surface waves can be generated by an active source, such as a hammer, weight drop,
 197 vibroseis, or by a passively recorded source, such as anthropogenic, traffic, or several other
 198 environmental sources (e.g., ocean waves, wind), and these waves are recorded by an array of
 199 geophones. Because surface waves can provide information on the subsurface velocities over a
 200 wide range of frequencies and wavelengths, the MASW technique can generate high-quality
 201 velocity models. MASW is often used to produce 1D velocity profiles, it can also be used to
 202 assess the lateral variability of the subsurface shear wave velocities, which is essential for
 203 characterizing subsurface heterogeneity and identifying areas of potential geotechnical concern.
 204 The MASW method can be applied in a wide range of geological environments and has the

205 advantages of being non-invasive, cost-effective, and capable of providing high-resolution V_s
206 profiles to depths of up to several tens of meters.

207 In active-source surface seismic surveys, over two-thirds of the total seismic energy
208 generated by compressional waves is transmitted to Rayleigh waves, sometimes referred to as
209 "ground roll" (Park et al., 1999b). An example of surface waves in our collected data is shown in
210 Figure 2a. Surface wave energy decays exponentially with depth beneath the surface. Longer
211 wavelength (i.e., longer-period and lower-frequency) surface waves travel deeper, thus
212 containing more information about deeper parts of the study area. Shorter wavelength (i.e.,
213 shorter-period and higher-frequency) surface waves travel shallower, thus containing more
214 information about shallower parts of the study area. Surface waves are dispersive, meaning each
215 wavelength propagates at different phase velocities in a layered medium. Thus, we can analyze
216 phase velocity of different frequency bands (corresponding to different wavelengths) and
217 estimate the velocity profile of the subsurface.

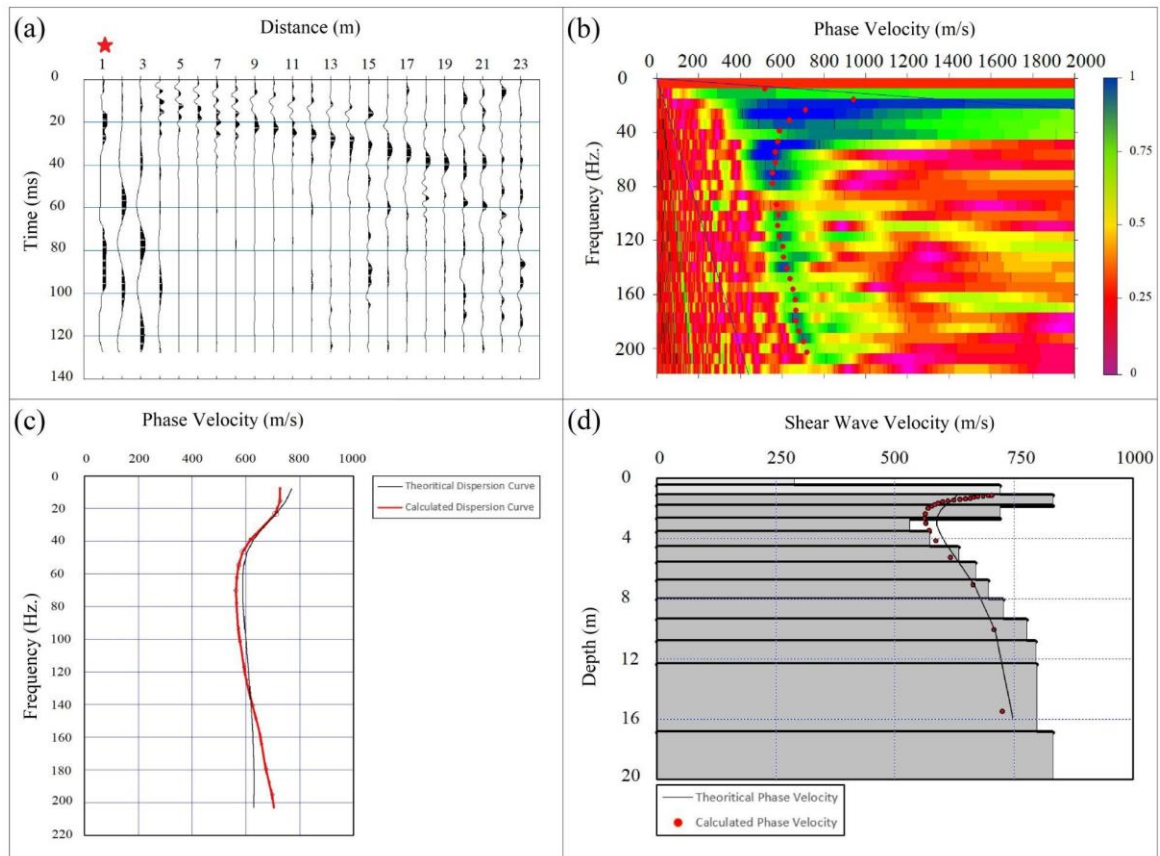
218 Rayleigh wave dispersion curves describe the velocity at which each wavelength travels.
219 To determine Rayleigh wave dispersion curves, we use the phase shift method, which provides
220 accurate fundamental-mode phase velocities even when only four geophones are used (Park et
221 al., 1999b; Dal Moro et al., 2003). Our detailed procedure is provided in Supporting Information.

222 Figure 2 represents an example of the inversion procedure for estimating a 1D velocity
223 profile. First, we applied a 7.50 - 327.68 Hz bandpass filter to all traces in a shot gather to
224 remove high-frequency noise, and we muted noisy traces (Figure 2a). Then, we calculated
225 dispersion images, determined phase velocities by picking the velocity with the maximum
226 amplitude at each frequency (Figure 2b), and extracted the fundamental mode velocity profile of
227 the Rayleigh surface wave from the dispersion image (Figure 2c). After wavelength-depth
228 conversion, we generated an initial model based on the phase velocity picks. Finally, a non-linear
229 least squares inversion method (Xia et al., 1999) was applied to the dispersion curve to
230 reconstruct the V_s velocity model (Figure 2d) using the SeisImagerSW software. The minimal
231 depth at which shear wave velocity can be reliably inferred through inversion is contingent upon
232 a confluence of site-specific variables. This interpretable depth is not a fixed measure but is
233 instead modulated by an array of factors, including the fidelity of seismic data, particularly its
234 high-frequency components, and the proximal spacing relative to the seismic source. Acceptable
235 final 1D models should have a root mean square (RMS) error of the difference between the
236 theoretical dispersion and measured dispersion curves (Figure 2c) below 5% (SeisImagerSWTM
237 Manual, 2009). With this procedure, we obtain an average 1D V_s vertical profile along the
238 seismic line.

239 For 2D V_s estimation, we carry out the same pre-processing, then we perform dispersion
240 analysis using the common mid-point (CMP) cross-correlation gathers. The CMP cross-
241 correlation method can increase the signal-to-noise ratio of the dispersion spectrum. A
242 comprehensive explanation of this method is provided by Hayashi & Suzuki (2004). Here, we
243 briefly discuss the following steps for CMP cross-correlation analysis: First, we calculate cross-
244 correlations between every pair of traces in each shot gather. Second, we collect correlation
245 traces with a common mid-point and stack those with the same spacing. The resultant cross-
246 correlation gathers resemble shot gathers and are known as CMP cross-correlation gathers.
247 Third, we calculate the dispersion image of surface waves using the MASW technique (Park et
248 al., 1999b) from the CMP cross-correlation gathers. Finally, for each CMP, we invert dispersion

249 curves for V_s models. As a general guideline, acceptable 2D models should result in an RMS
 250 below 15% (SeisImagerSWTM Manual, 2009).

251 MASW is limited to shallow depth investigations, typically up to 30 meters. Beyond this
 252 depth, the resolution and accuracy of the method decrease significantly. Moreover, MASW is
 253 more suitable for homogeneous soil conditions and struggles to characterize laterally varying
 254 structures or complex geological settings accurately (Boiero & Socco, 2011; Evangelista &
 255 Santucci de Magistris, 2015). To overcome these limitations in the future, seismic refraction or
 256 reflection could be employed over a larger region as a complementary technique, although
 257 reliable picking of the un-aliased arrivals in this complex near-surface zone will likely require
 258 more than 24 geophones and a high-frequency seismic source. The depth and compression
 259 velocity information of different subsurface layers can be determined by analyzing the travel
 260 time data. Seismic refraction has the advantage of investigating deeper depths, making it useful
 261 for studying subsurface structures beyond the reach of MASW. The material in section S2 of the
 262 Supporting Information can serve as a basis for a future permafrost study combining MASW and
 263 seismic refraction. Advances in data acquisition and processing should be taken into account to
 264 ensure the best possible outcomes in future investigations. By integrating the strengths of these
 265 two techniques, it may be possible to enhance the accuracy and depth range of permafrost
 266 characterization.



267

268 **Figure 2.** The procedure of building V_s models from extracted dispersion curve using MASW
 269 method: (a) The pre-processed shot-gather (Red star represents the shot location), (b) The

270 calculated dispersion image representing Rayleigh wave phase velocity for each frequency (Red
271 dots represent picks at high amplitudes), (c) The extracted dispersion curve from the dispersion
272 image, and (d) V_s model inverted from the dispersion data.

273 3.2 Electrical Resistivity Tomography Method

274 Surface electrical resistivity surveying is based on the principle that the distribution of
275 electrical potential in the ground around a current-carrying electrode depends on the electrical
276 resistivities and distribution of the surrounding soils and rocks. The usual practice in the field is
277 to apply an electrical direct current (DC) or alternating current (AC) of low frequency. The
278 voltage between two potential electrodes and the current between two other electrodes are
279 measured during the ERT survey. Measurements were provided using various pairs of electrodes
280 along the transect. An increase in spacing between electrodes allows for deeper investigation
281 depth. Therefore, apparent resistivity values can be obtained through the voltage, current, and
282 geometry of array electrodes for each point laterally and with depth. The measured apparent
283 resistivity values are used in the inversion to obtain resistivity models for subsurface material.

284 After data acquisition, the data was checked for large measurement errors (>2%) using
285 Prosys II software (IRIS Instruments), which was provided with the Syscal equipment. During
286 the data acquisition process, a roll-along technique was implemented, involving the relocation of
287 the array's center to a distance of 18 m (approximately half of the initial length equal to 35.5
288 meters). To assess the quality of the data, we computed the errors between measurements taken
289 after this center movement. Approximately 20% of the total measurements were repeated, and
290 the average error was found to be less than 1%. These metrics provide valuable insights into the
291 overall data quality, indicating a relatively low average error and the redundancy of about 20% in
292 the measurements. For the purpose of joint inversion, we combined Wenner-Schlumberger (WS)
293 and Dipole-Dipole (DD) data into one dataset.

294 Res2Dinv software (Res2Dinv Manual, 2006) was used to generate a resistivity model
295 from apparent resistivity values. The inversion software uses a smoothness-constrained least
296 squares method with L2-norm (Loke et al., 1996). For the model mesh, we used half-electrode
297 spacing (0.25 m) in the horizontal direction. In the vertical direction, the thickness for the first
298 layer was set to 0.125 m with a 1.1 factor to increase thickness with depth.

299 The inverted resistivity model can also be influenced by topographic changes along a
300 transect, particularly on the top cells. Minor variations in topography may have negligible effects
301 on the inversion process, but substantial changes can introduce distortions. Elevation changes
302 along the transect are generally insignificant and less than 0.5 meters on the edges of ice wedges
303 polygons for our site. As a result, topography has not been integrated into the inversion process.
304 In some cases, degraded polygons have large elevation changes, and it is crucial to carefully
305 evaluate the significance of topographic changes for these areas when dealing with geophysical
306 inversion models.

307 We used robust constraint and defined an initial half-space resistivity value of 10 Ωm to
308 trace spatial cryopegs distribution based on low resistivities observed in previous studies
309 (Hubbard et al., 2013; Overduin et al., 2012; Yoshikawa et al., 2004). A 2D ERT model was
310 generated to invert WS and DD arrays jointly, and the result achieved an RMS error of 1.8%.
311 Across different iterations, specifically the 3rd, 4th, and 5th, the percentage changes were 5.8%,
312 2.8%, and 1.86%, respectively. When comparing the results of inverted resistivity with varying

313 RMS errors, notable variations were observed primarily in the lower cells of the model. The
 314 overall changes between the 4th and 5th iterations were evident in both resistivity and the bottom
 315 boundary for the deepest contrast layer. Nonetheless, these changes remained generally stable
 316 and did not substantially affect our interpretation results.

317 ERT and other electromagnetic methods give us inherently non-unique solutions for
 318 mapped reconstructions of subsurface electrical properties. This non-uniqueness means that the
 319 measured data can be explained equally well by multiple models. To improve the reliability of
 320 subsurface interpretations, we use soil core sampling and comparison with other geophysical
 321 methods, such as the MASW technique.

322 3.3 Correlation of Soil Mechanical Properties with Shear Wave Velocity

323 Soil's mechanical properties can be determined using V_s , which is a commonly used
 324 geotechnical and geophysical parameter. There are empirical or analytical correlations between
 325 V_s and several other soil properties. For instance, there is a positive correlation between V_s and
 326 soil stiffness parameters such as shear modulus (G) and elastic modulus (Young modulus) (E).
 327 Stiffer soils generally exhibit higher shear wave velocities and are correlated with higher soil
 328 strength parameters such as undrained shear strength (S_u) and peak shear strength. In addition, V_s
 329 is inversely correlated with soil porosity, where lower V_s values are often observed in soils with
 330 higher porosity. For a given soil type, with constant parameters like temperature and ice content,
 331 V_s is directly proportional to soil density, indicating that denser soils generally exhibit higher V_s
 332 values. Furthermore, soil classification, which determines the foundation design, directly
 333 correlates with V_{s30} and S_{u30} , which are the averages of V_s and S_u in the top 30 meters (ASCE/SEI
 334 7-16, 2017). Therefore, understanding the soil classification and V_s is crucial for assessing the
 335 seismic performance and stability of foundations and for designing appropriate foundation
 336 systems.

337 For soil that is elastic, isotropic, and homogeneous, the elastic theory can be used to
 338 establish the following relationship between elastic modulus and seismic wave velocity:

339

1)	$\mu = \frac{\left(\frac{V_p}{V_s}\right)^2 - 2}{2\left(\frac{V_p}{V_s}\right)^2 - 2}$
----	--

340

2)	$G = \frac{\gamma V_s^2}{g}, \text{ and}$
----	---

341

3)	$E = 2G(1 + \mu),$
----	--------------------

342 where, μ is the Poisson's ratio, γ is the unit weight of the media, and g is the gravitational
 343 acceleration, which can affect the foundation design in various ways such as foundation type,
 344 foundation settlement, and allowable vertical and lateral loads (Coduto, 1999). The relationship

345 between elastic modulus and bearing capacity of soils could depend on several factors such as
 346 soil classification, stress history, foundation type, etc. The elastic settlement beneath a flexible
 347 footing placed on the ground surface can be calculated as follows (Terzaghi et al., 1996):

$$(4) \quad S_e = \frac{qB(1-\mu^2)I_f}{E},$$

348 where q is the surcharge load, B is the width of the footing, and I_f is the influence
 349 factor, which is a function of the ratio of length to width ($\frac{L}{B}$) and the thickness of the
 350 compressible layer. We will highlight the importance of V_s monitoring on change in elastic
 351 modulus and elastic settlement in subsection 5.6.

352 4 Data Acquisition

353 There are eight seismic survey locations using MASW, six temperature measurement
 354 locations using thermistors, one ERT survey location (at MASW 3 location), and five core
 355 sampling locations (at Roadside and MASW 1-4 locations), as shown in Figure 1. The
 356 coordinates of these locations are provided in Table S1 in the Supporting Information. The
 357 seismic surveys cover various soil conditions, including disturbed and undisturbed areas. Four
 358 seismic surveys (MASW 1-4) were performed on undisturbed tundra permafrost and four
 359 (Roadside and NOAA 1-3) on disturbed permafrost, shown in Figure 1c. The seismic surveys
 360 performed on disturbed permafrost include one survey along the gravel road near the National
 361 Oceanic and Atmospheric Administration (NOAA) facility (Roadside), one survey under the
 362 NOAA building (NOAA 1), one survey on the pre-existing building foundation next to the
 363 NOAA building (NOAA 2), and one survey on the tundra near the pile foundations (NOAA 3).
 364 At the NOAA 2 location, a building was demolished and removed one year prior to the seismic
 365 survey, but the pile foundations remain in the ground. The core sampling was performed at
 366 approximately 1 m from the seismic survey locations using a hand-held sampling drill. The
 367 sampling depth is up to 1.5 m.

368 4.1 Surface Wave Data Acquisition

369 Each seismic line consists of 24 vertical 4.5 Hz geophones (a 24-channel Geometrics
 370 Geode seismograph) positioned on the ground surface. Straight-line seismic profiles have
 371 geophone spacing equal to 1 m, which gives us a 23 m spread in total. We generated seismic
 372 signals using a sledgehammer adjacent to the geophones as well as an extra shot at 5 m offset
 373 from the beginning of the lines. The seismic record length was 128 ms with a sample interval of
 374 0.25 ms, and each recording was initiated by a trigger attached to the sledgehammer. No pre-
 375 acquisition filter was used on the seismic data. Note that with the vertical source and the vertical
 376 receivers, the type of surface waves we acquired are Rayleigh waves. An example of the
 377 collected seismic traces is shown in Figure 2a.

378 4.3 Temperature Data Acquisition

379 Small holes with 0.02-m diameter were punched in the ground to a depth of 1.5 meters in
 380 August 2021. Four HOBO TMC6-HD temperature sensors were then lowered into the ground
 381 using wooden rods to the depth of 0.02, 0.2, 0.5, and 1.5 m below the surface. At each location,
 382 temperature sensors were connected to two 2-channel HOBO U23-003 loggers in September
 383 2022 (Supporting information). The operating temperature range for loggers is -40 to 100 °C

384 with an accuracy of 0.4 °C and 0.2 °C below and above 0 °C, respectively. The resolution is 0.02
385 °C. Data records were collected during the field trip in August 2022. Because most of the
386 commonly used construction materials are prohibited in this study area, reducing the
387 vulnerability of the sensor installation to damages by wildlife animals is a challenging task and
388 several temperature sensor cables were severed by Arctic foxes. Nevertheless, temperature
389 records were collected at the six following sites. Site conditions were described during
390 installation as follows. The Temp 1 profiler was placed into a shallow pond with 10 cm of
391 standing water; The Temp 2 profiler is located near a rim of the flat-center ice-wedge polygon;
392 the site conditions could be described as moist. The Temp 3 station is placed at the center of a
393 high-center polygon with a dry ground surface. The Temp 4 site is almost saturated, with a thin
394 layer of standing water in the middle of the low-center polygon. The Temp 5 profiler is at the rim
395 of the low-center polygon, with the dry ground around it. Finally, the Temp 6 profiler is
396 approximately 9 m from shore, where the ground is rather moist.

397 4.4 Electrical Resistivity Tomography Data Acquisition

398 An Electrical Resistivity Tomography (ERT) survey was conducted to provide in-situ
399 resistivity measurements (Ωm) along the MASW 3 transect from September 13, 2022. The ERT
400 station Syscal-Pro 72 (IRIS instruments) and steel electrodes were used to acquire data.
401 Electrodes were placed along the transect using measuring tape with a 0.5 m spacing. Inverse
402 WS and DD arrays were applied for measurements. The minimum/maximum half electrode
403 spacing was 0.75m/17.25m for WS and 0.5m/13.5 m for the DD array. A 50 V output voltage
404 and 250 ms pulse duration were applied during the survey. Contact resistances for most of the
405 electrodes were no more than 1 k Ω . Measurements with errors exceeding 2% were removed
406 during processing.

407

408 5 Results and Discussion

409 The following subsections provide an overview of the V_s , electrical resistivity, and
410 temperature results. We highlight key results related to permafrost, including site
411 characterization (5.1), shear wave velocity interpretation (5.2-5.4), civil infrastructure's influence
412 on permafrost (5.5), and applications to engineering properties and infrastructure design (5.6).

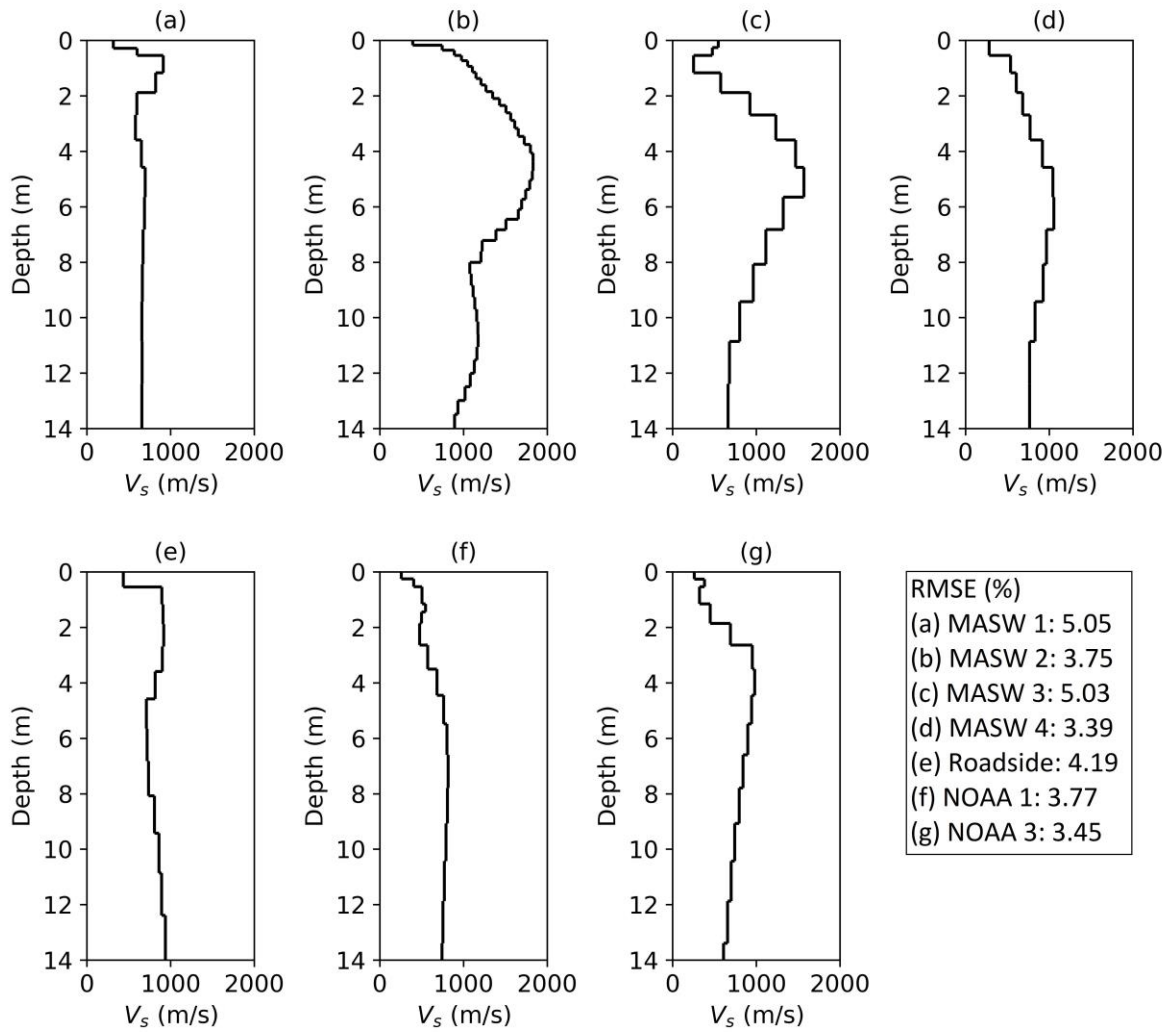
413 5.1 Site characterization of disturbed and undisturbed permafrost

414 We calculated 1D and 2D V_s models for 8 survey lines after performing inversion on the
415 calculated dispersion curves using the MASW method (Park et al., 1999a, 1999b). This included
416 both disturbed and undisturbed permafrost regions. Figure 3 shows the 1D V_s profiles for the
417 survey locations on the tundra, which are categorized as undisturbed permafrost locations. Figure
418 3a shows the V_s profile for the first location of MASW survey in the tundra (MASW 1),
419 approximately 500 meters from the road and NOAA facility. A similar V_s profile is observed in
420 Figures 4b-d, except that the relative high-velocity zone is located relatively at a lower depth and
421 has a more consistent velocity profile at higher depths than MASW 1. This could be an effect of
422 the different geology, vegetation, or the effect of anthropogenic activities over the years, as we
423 observed many marked points for previous studies and tracks from vehicles in the field. Figure
424 3b represents the V_s for the second location in the tundra (MASW 2), approximately 1 km from
425 the infrastructure. We observe a very high-velocity zone at a depth of 2-8 meters below the

426 surface, representing either a stiff lithology layer or an ice-rich zone. The highest V_s layers are
427 located at a depth of 5 meters and are as high as 1700 m/s. This location clearly shows the
428 undisturbed permafrost area with higher V_s and higher ice content. Figure 3c illustrates the
429 velocity model for the third location in the tundra (MASW 3), roughly 1.5 km from the road and
430 NOAA building. While the low-high-low V_s pattern is obvious, the highest velocity is 1575 m/s,
431 which is lower than that at the MASW 2 at 1 km. In the field, we observed that as we get further
432 to the tundra, the ground gets wetter as indicated by many ponds in the area. This can also be
433 seen on the satellite map in Figure 8c-d (presented later in this paper), where the last two lines
434 (MASW 3 and 4) are located in darker areas that represent higher surface water content. Figure
435 3d illustrates the velocity model for the last location in the tundra (MASW 4) at roughly 2 km
436 from the road and NOAA building. Like all other locations in the tundra, we observed the low-
437 high-low velocity profile, but the highest velocity zone is located at deeper depths of 7 meters. In
438 addition, the highest V_s is 1150 m/s at MASW 4, which is lower than those at the two previous
439 locations in undisturbed permafrost zones (MASW 2 and 3). These last two locations (MASW 3
440 and 4) represent the effect of vegetation and high surface water content. The previously observed
441 low-high-low velocity profile below the surface by Dou & Ajo-Franklin (2014) is captured at all
442 tundra locations (i.e., MASW 1-4 and NOAA 3).

443 Figures 3e-g show the 1D V_s profiles for the survey locations near the NOAA building,
444 including the roadside, within 1.0 meter of the NOAA building (NOAA 1), and ~80 meters away
445 from the NOAA building (NOAA 3), where we expect high disturbance in permafrost. These
446 locations are categorized as disturbed permafrost locations. The V_s at disturbed permafrost
447 locations is lower than that at undisturbed permafrost locations, as the vegetation and thus albedo
448 are affected by human activities, and the ice content is lower than that in the undisturbed
449 permafrost region. Figure 3e represents the V_s for the location within 1.0 meter of the gravel road
450 leading to the NOAA facility, where we expect high disturbance in permafrost. The 1D velocity
451 profile represents a low-high-low velocity pattern with the highest V_s of 850 m/s. It is noted that
452 the data at the pre-existing demolished building foundation next to the NOAA building (NOAA
453 2) are low-quality, which resulted in higher RMS error than the acceptable error. As we
454 performed sledgehammer shots on top of a pre-existing building foundation, the contrast in soil
455 and pile material properties and the resulting scattered energy likely generated relatively larger
456 errors than in other locations.

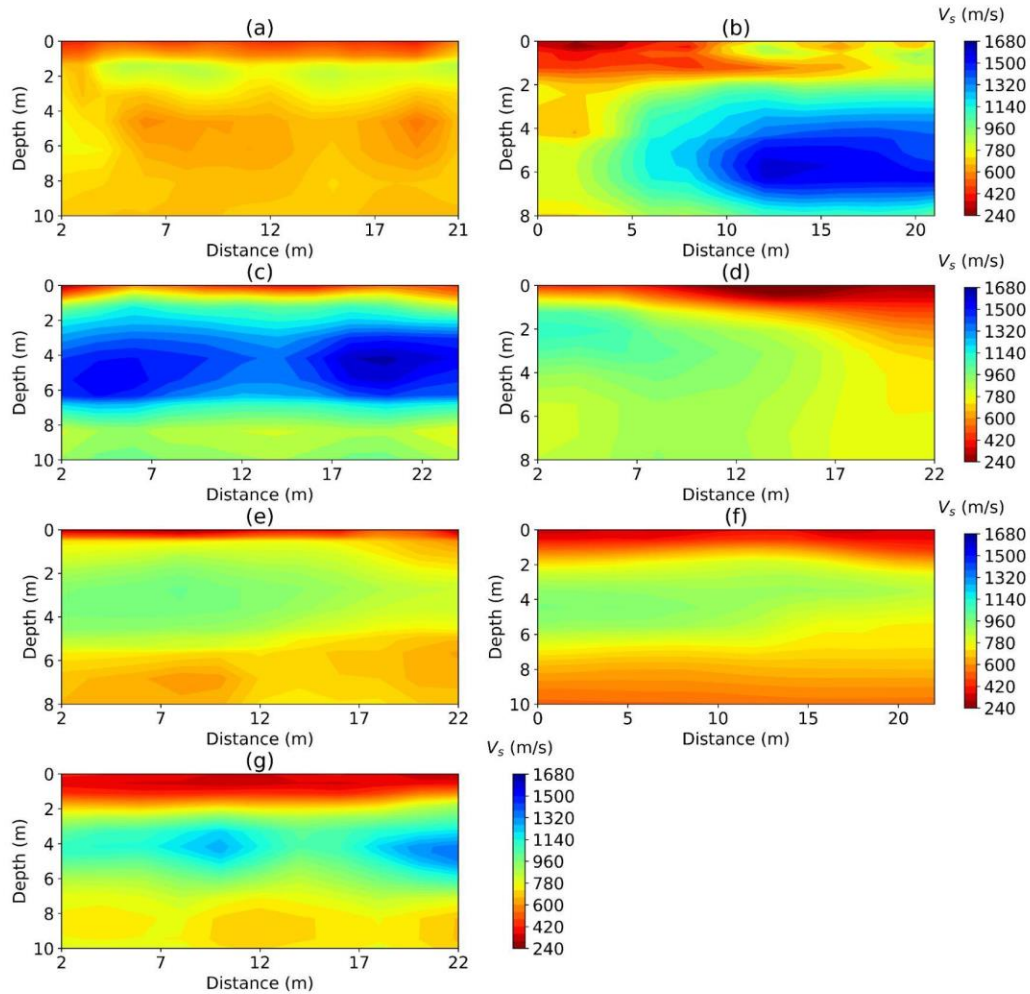
457 Figure 4 shows the 2D V_s models in the undisturbed (4a-d) and disturbed (4e-g)
458 permafrost regions similar to Figure 3. A low-high-low velocity pattern is evident in all models,
459 indicating the active layer and transitional zone (with low velocity), ice-rich permafrost (with
460 high velocity), and partially frozen permafrost with scattered ice (low velocity). Previous studies
461 have shown a strong correlation between permafrost temperature and V_s (Ji et al., 2023; Kurfurst,
462 1976; Nakano et al., 1972). The low-high-low velocity pattern is consistent with the general
463 trend of permafrost temperature variation with depths, as in a previous study (Smith et al., 2022).
464 Although the velocity and depth vary spatially, the low-high-low pattern is consistent among all
465 locations. The 2D models capture the spatial variability of permafrost, demonstrating the
466 importance of multichannel seismic surveys and 2D modeling. We will discuss these models in
467 detail in sections 4.2 and 4.3.



468

469 **Figure 3.** 1D V_s profiles for undisturbed (a-d) and disturbed (e-g) permafrost locations: (a)
 470 MASW 1, (b) MASW 2, (c) MASW 3, (d) MASW 4, (e) Roadside, (f) NOAA 1, and (g) NOAA
 471 3.

472



473

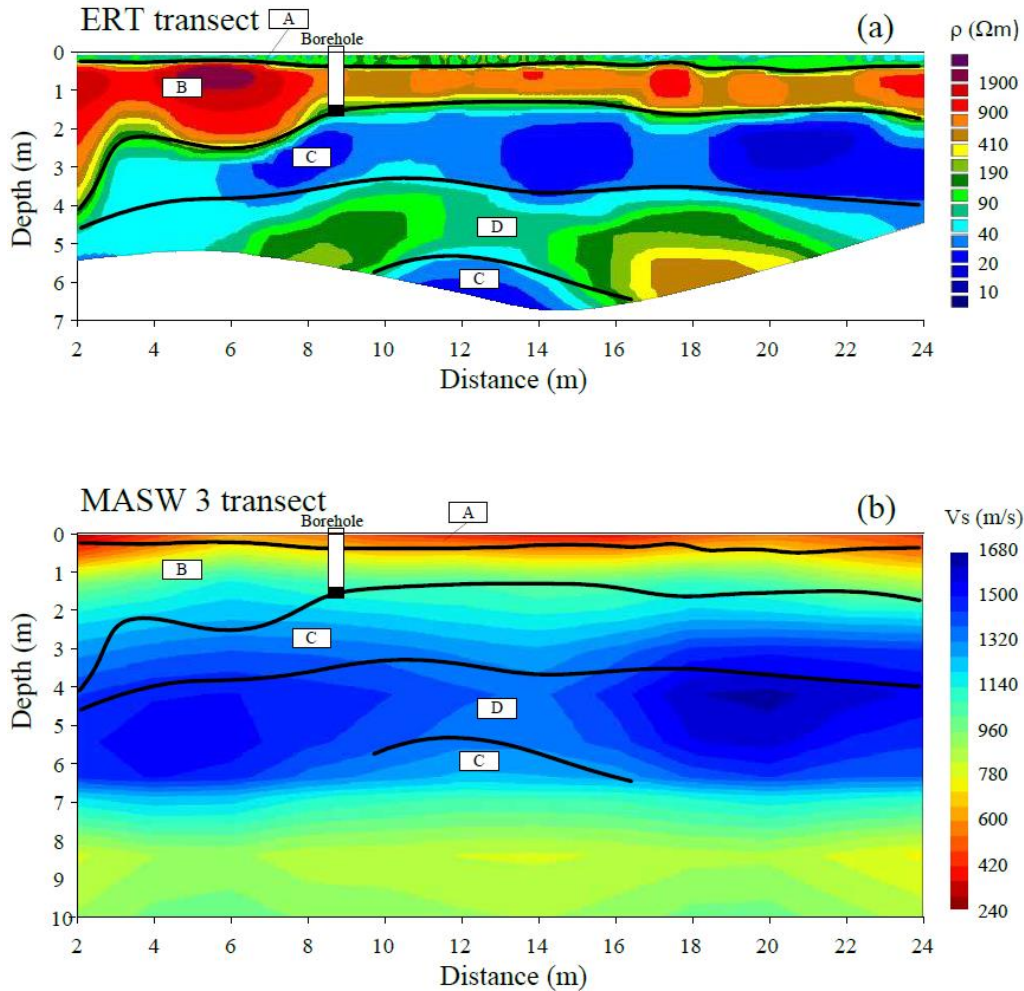
474 **Figure 4.** 2D V_s profiles for undisturbed (a-d) and disturbed (e-g) permafrost locations: (a)
 475 MASW 1, (b) MASW 2, (c) MASW 3, (d) MASW 4, (e) Roadside, (f) NOAA 1, and (g) NOAA
 476 3.

477

478 Meanwhile, we invert the electrical resistivity model (in Figure 5a) from the ERT data,
 479 which can delineate several zones compared to the V_s model from the MASW 3 transect (Figure
 480 5b). Each zone is characterized by different thicknesses, electrical resistivity, and velocity
 481 values. Zone A is characterized by relatively low resistivity up to 200-300 Ωm from the surface
 482 down to approximately 0.4 m. This layer represents the active layer and is characterized by low
 483 V_s of 240 m/s. Zone B is characterized by high resistivity values of 400-2000 Ωm . The thickness
 484 of this layer varies from 1 m at distances of 6-24 m to 4 m at distances 2-6 m. According to
 485 drilling data, the zone between 1.4 m and 1.7 m is a transition zone (black box marked in the
 486 borehole in Figure 5) between a frozen and unfrozen state and represents a boundary between
 487 zone B and C. Zone C is characterized by soils with low resistivity of 10-20 Ωm associated with
 488 cryopegs development in the study area. The thickness of the layer is about 2.5 m along the

489 profile and decreases toward the beginning of the transect. At a depth of 0.5-0.6 meters, the
490 salinity measured approximately 0.84 ppt (parts per thousand, roughly equivalent to grams per
491 liter). In contrast, at a deeper level, specifically 1.5-1.6 meters, the salinity was significantly
492 higher, measuring 8.03 ppt. Consequently, one can infer that salinity gradually increases from
493 Zone B to Zone C, contributing to the low resistivity observed for cryopegs in Zone C. The
494 characteristics of Zone C, exhibiting low resistivity and relatively high velocity, may be
495 attributed to two potential factors. Firstly, it is plausible that this zone remains frozen, with its
496 temperature lingering below the freezing point of cryopegs. Alternatively, the distinct lithology
497 and soil mineral composition within this zone could be significantly influencing the resistivity
498 and seismic velocity properties of unfrozen sediments in the near-surface, as highlighted in
499 studies by Rossi et al. (2022) and Accaino et al. (2023), respectively. These findings are aligned
500 with previous studies demonstrating the complex and heterogeneous nature of permafrost in the
501 study site (Brown, 1969; Dafflon et al., 2016). Zone D is characterized by relatively high
502 resistivity values of 100–600 Ωm and a thickness of approximately 2m and is located between
503 two zones of low resistivity (both zones denoted as Zone C). The zone is also characterized by
504 high V_s up to 1600 m/s, typical for frozen material and increased ice content. Due to the
505 relatively high-velocity values, the high-resistivity layer D, and the presence of salt pockets even
506 in ice-rich conditions in Utqiagvik (Iwahana et al., 2021), we interpret this layer as an ice-rich
507 layer. High-velocity values for zone D are also supported by the intra-ice brine pockets, where
508 cryopeg brine is bounded by ice, and are generally in solidified form (Iwahana et al., 2021).

509 Due to the high contrast of the resistivity of different units, the ERT method helps to
510 identify multiple layers in the upper part of the cross-section that cannot be clearly distinguished
511 using the MASW method due to the lack of high-frequency signals. The MASW results provide
512 useful information to verify ERT results at greater depths. The MASW method reveals a high
513 degree of heterogeneity in the permafrost, possibly due to increased salinity at greater depths,
514 resulting in unfrozen zones. Additionally, integrating ERT and MASW provides a more
515 comprehensive assessment, offering insights into critical aspects, such as the salinity and ice
516 content within the permafrost, which are crucial for understanding its physical properties and
517 behavior. This methodological framework, effective in our specific study area, has potential
518 applicability in diverse permafrost environments, indicating its potential for wider application
519 and enhancing the knowledge of near-surface permafrost dynamics.



520

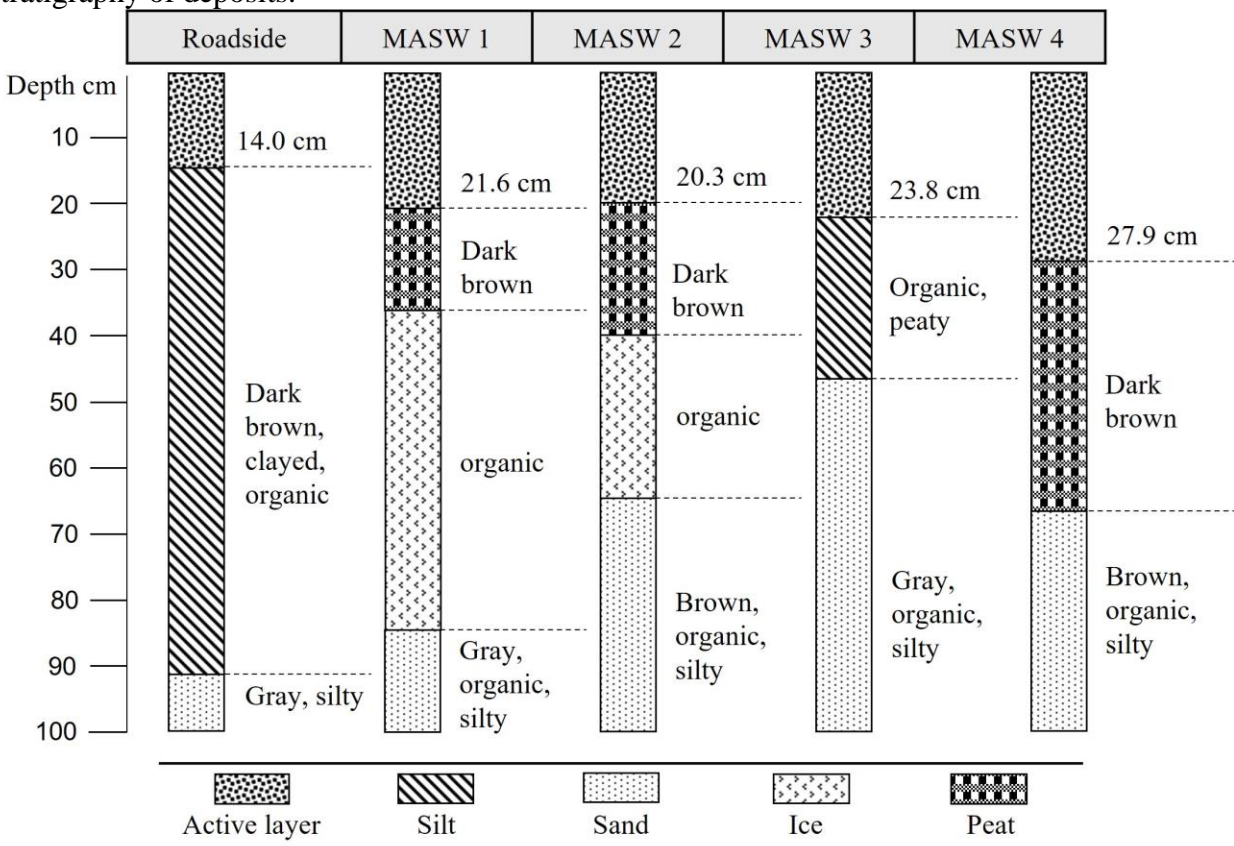
521 **Figure 5.** 2-D ERT (a) and MASW (b) comparison results at the MASW 3 location. Black lines
 522 represent interpreted ERT boundaries based on resistivity values. Zones A to D specify different
 523 ranges of electrical resistivity and shear wave velocity values corresponding to various
 524 permafrost structures. The white box indicates the borehole sample, and the black box inside the
 525 white box shows the transition zone.

526

527 5.2 Identification of active layer thickness

528 Significant variations in ALT exist between different landscape types, reflecting the
 529 influence of vegetation, substrate, microtopography, and especially soil moisture (Shiklomanov
 530 et al., 2010). From V_s profiles shown in Figure 4, we can identify the ALT range (roughly 0.3 m)
 531 and the shear wave velocities of the active layer (240 – 370 m/s) in most locations. However, in
 532 some undisturbed permafrost regions, ALT was found to be highly spatially heterogeneous due
 533 to differences in subsurface characteristics based on 2D V_s profiles shown in Figure 4. Therefore,
 534 ALT at some locations may be 0.5 – 0.6 m, which is consistent with the ALT range estimated
 535 from nearby temperature measurements (described in Section 2.3) and the earlier estimation by
 536 Jafarov et al. (2016). In contrast, ALT in disturbed permafrost regions presents higher values (0.5
 537 – 1.0 m) and less spatial heterogeneity. The higher ALT indicates that the ground temperature is

538 slightly higher for the permafrost with human activities than in the undisturbed permafrost. For
 539 NOAA 1 (Figure 3f), the high consistency in ALT is because the ground surface is under the
 540 NOAA facility, and the topsoil is gravel, which is different from all other locations. The
 541 coverage of the building, which produces continuous heat, and the high thermal conductivity of
 542 gravel compared to fine-grained soil like peat or silt are likely contributing factors to the
 543 temperature consistency of the tested line. The MASW results did not reveal the top shallow
 544 active layer of MASW 3 due to the small ALT (0.24 m based on soil sampling) and lack of high-
 545 frequency source signal required to image shallow depths. Figure 6 illustrates the stratigraphy of
 546 deposits up to 1.0 m at the five sampling locations. The permafrost mainly consists of silty soil
 547 with organics with an average unit weight of 19.62 kN/m^3 . Ice layers are evident in the boreholes
 548 of MASW 1 and 2. Based on the boring samples collected at the same sites of the seismic
 549 surveys, ALT in the study regions were 0.14 – 0.28 m during sampling. The ALT range
 550 identified by MASW in most locations is within a reasonable range compared with the
 551 stratigraphy of deposits.



552

553 **Figure 6.** Stratigraphy of borehole core samples at five locations.

554

555

5.3 Identification of spatial heterogeneity of permafrost

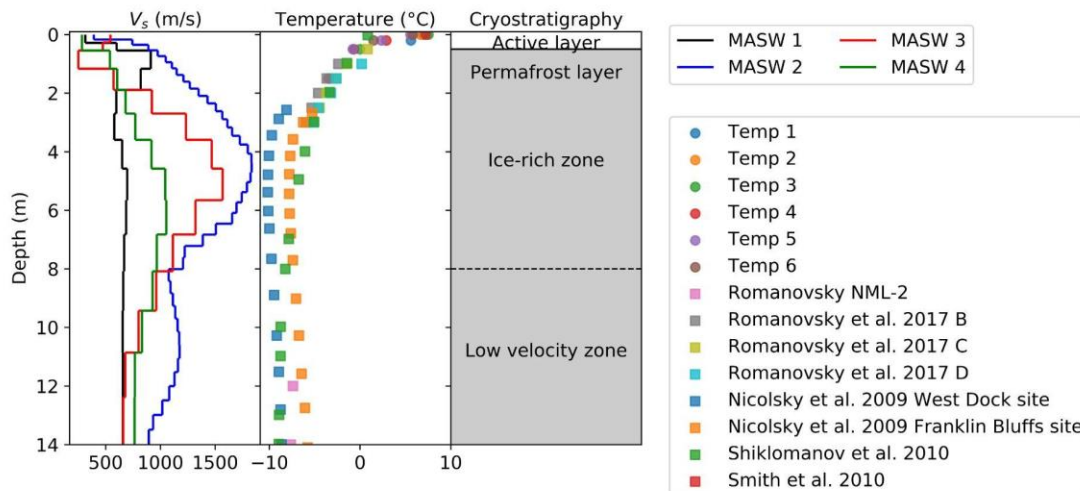
556 Spatial heterogeneity within the permafrost layer can be observed and quantified by
 557 analyzing V_s profiles, including ice-rich permafrost, low-velocity zones, and cryopeg. Shear
 558 wave velocities within the permafrost layer range from 450 to 1700 m/s. The shear wave
 559 velocities of ice-rich permafrost zones (MASW 2-4) are in the range of 700 – 1700 m/s, which is

560 higher than the range of 500 – 900 m/s from other permafrost locations. Ice-rich permafrost can
 561 be identified in 2D V_s profiles, such as in Figure 4b (MASW 2), with a high-velocity zone (from
 562 9 m to 22 m) with a V_s range of 1300 – 1700 m/s. The theoretical V_s of pure ice is approximately
 563 1900 m/s at a temperature near -10 °C (Kohnen, 1974). Given that the effective V_s of a medium
 564 is a weighted average of the components of that material, the regions of the subsurface with
 565 velocities near 1700 m/s are expected to be ice-rich materials. This indicates that the center area
 566 of the ice-rich zone is likely composed primarily of ice layers. However, the gradual increase of
 567 the velocity near the ice-rich zone at MASW 2 indicates suspended soil around the ice layers.

568 Bodies of unfrozen material, taliks or cryopegs, can also be identified using V_s profiles.
 569 For example, a cryopeg layer exists at MASW 3 at a depth of 1.2 – 1.6 m with a corresponding
 570 V_s of 250 m/s. The boring log information at MASW 3 shows that the sediments gradually
 571 change from frozen to unfrozen state at depths of 1.2 – 1.6 m. Figure 1c shows that MASW 3 is
 572 located in a wetter area (darker image color is related to higher surface water content), which
 573 may lead to open talik regions around the large water body. Another potential reason for this
 574 talik or cryopeg layer is salinity, as higher salinity layers exist at MASW 3 due to proximity of
 575 the nearby saline thermokarst lake. This is consistent with our observation of core sample's
 576 salinity at MASW 3 (discussed in subsection 5.1). The V_s range of the cryopeg layer
 577 (approximately at 1.5 m) is similar to that of the active layer since the cryopeg layer may be
 578 unfrozen.

579 5.4 Impacts of ground temperature and ice structure on shear wave velocities

580 In subsections 4.4 and 4.5, we focus on the impacts of multiple factors on shear wave
 581 velocity in undisturbed permafrost to better understand permafrost behavior and stability. Figure
 582 7 shows the composed profiles of V_s in undisturbed permafrost, temperature variation, and
 583 cryostratigraphy versus depth. The temperature difference between adjacent locations decreases
 584 with depth. The temperature measurements are derived from several locations near Utqiagvik,
 585 Alaska. The detailed location and record date of the temperature measurement are presented in
 586 Figure S2 and Table S2 in the Supporting Information. The temperature reveals that the ALT is
 587 around 0.5 m, which agrees with the ALT determined from the MASW surveys.



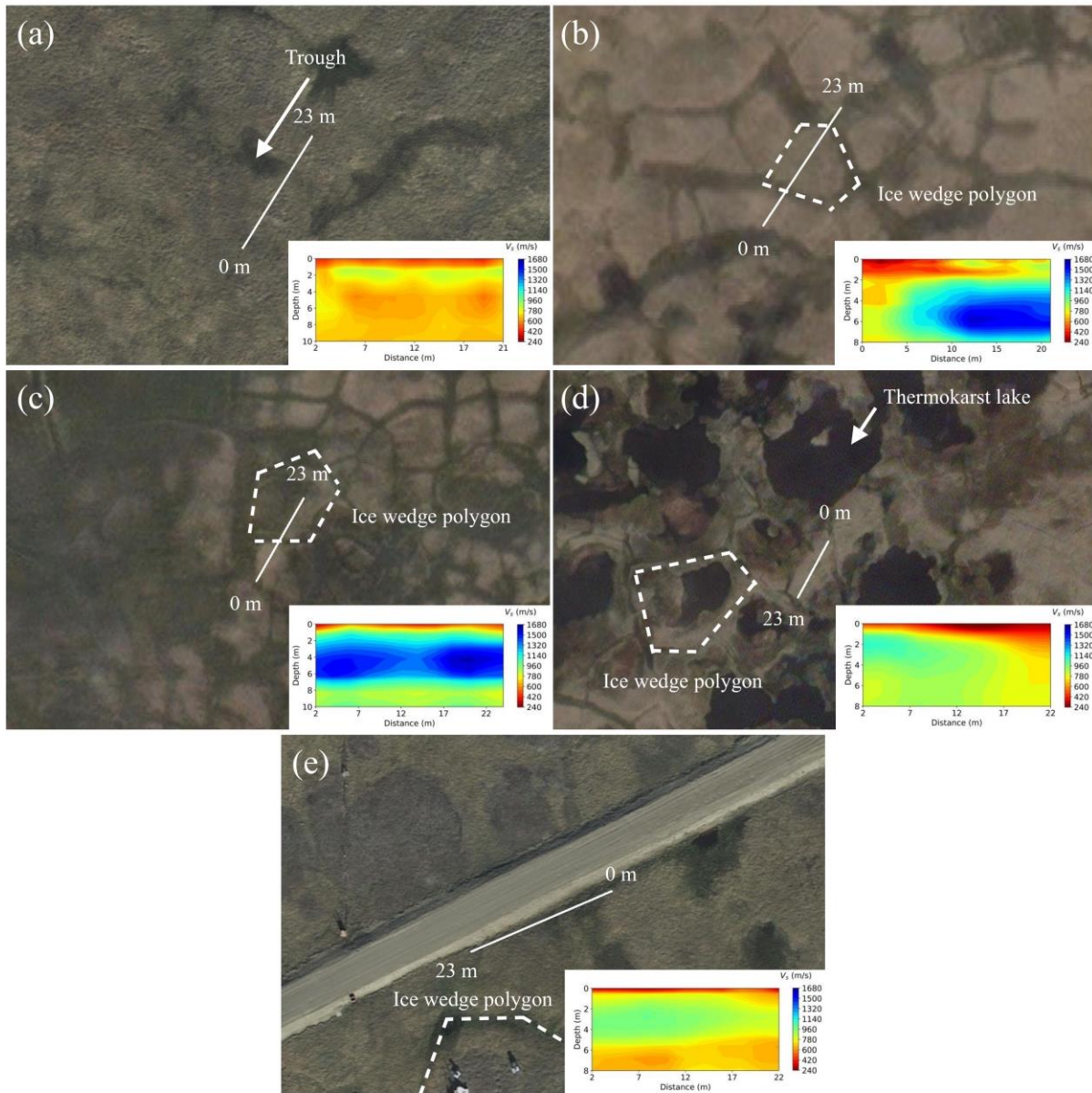
588

589 **Figure 7.** Composed velocity, temperature and stratigraphy profiles near Utqiagvik, Alaska.

590

591 We observed that the depth variation of V_s exhibits a consistent trend across different
592 testing locations near Utqiagvik (see Figure 7). The V_s is low ($\sim 250 - 510$ m/s) in the active
593 layer and increases in the permafrost layer to around $1200 - 1700$ m/s as depth increases to $5 - 8$
594 m. Beyond this depth, the shear wave velocities decrease, forming a low-velocity permafrost
595 zone ($\sim 500-700$ m/s) beneath the high-velocity permafrost layer. Dou and Ajo-Franklin's (2014)
596 study also reported the existence of a low-velocity permafrost zone at a location approximately 5
597 km south of the study area. This suggests that low-velocity permafrost zones may exist under the
598 tundra near Elson Lagoon and east of Utqiagvik, Alaska. As shown in Figure 7, the V_s profiles
599 are correlated with temperature profiles, with higher ground temperature corresponding to lower
600 shear wave velocities of permafrost. We also observe that V_s below 8 meters decreases, possibly
601 due to discontinuous ice in deeper zones. Based on the 1D and 2D velocity profiles, we conclude
602 that generally, the $2-8$ m zone contains higher ice connectivity (and therefore less scattered or
603 discontinuous ice), which causes very high-velocity zones. This can clearly be seen in 2D plots
604 where a high-velocity zone (and not a continuous layer) exists on the undisturbed permafrost
605 velocity profiles (Figures 4b and 4c). Therefore, although the temperature can be consistent in
606 higher depths (as shown in Figure 7 using the literature datasets collected in Utqiagvik, AK), the
607 velocity could be different due to changes in ice content and the spatial distribution of ice. While
608 the temperature profiles closely align with each other, there are clear disparities exist in the V_s
609 profiles. Such differences might be indicative of pronounced lateral variations in ice content or
610 could reflect changes in the lithology or texture of the underlying sediments.

611 Ice-wedge polygons occur on nearly all nearshore land surfaces (Kanevskiy et al., 2013)
612 and can be outlined using 2D V_s profiles. The formation and degradation of these polygons are
613 linked to climate change, resulting in severe landscape alteration. There are mainly three types of
614 ice-wedge polygons in the tundra between Utqiagvik and Elson Lagoon: high-centered polygons,
615 flat-centered polygons (incipient polygons), and low-centered polygons. High-centered polygons
616 are shown in Figure 8b, flat-centered polygons in Figure 8c, and low-centered polygons in Figure
617 8d, surrounded by thermokarst lakes. An early stage of high-centered polygon formation can be
618 seen in Figure 8a. MASW 4 is surrounded by coalescent low-center polygons (Lara et al., 2015)
619 and thermokarst lakes based on the satellite view nearby (Figure 8d), presenting lower V_s
620 compared with high-centered polygon regions (Figure 8b). The landscapes near MASW 4
621 develop and degrade from flat-centered and high-centered polygons (Nitzbon et al., 2019),
622 showing severe landscape alteration due to climate change. This transformation is referred to as
623 ice-wedge polygon degradation. A water body in the center of the low-centered polygons can
624 change the hydrological regime of polygon nets and lead to the onset of thermokarst activity
625 (Kartozii, 2019). As shown in Figure 8b, some of the high-centered polygons are developing
626 and connecting, presenting ice-rich permafrost zones with high V_s , which have the potential to
627 form thermokarst lakes during permafrost degradation. MASW 2 and 3 cover the polygon
628 centers and troughs of high-centered polygons, while MASW 4 is on the rim between
629 thermokarst lakes. For locations with surface water, V_s presents lower values on the top of the
630 permafrost layer than adjacent permafrost.



631
 632 **Figure 8.** Satellite view of MASW testing locations in undisturbed permafrost tundra and
 633 disturbed permafrost roadside: (a) MASW 1 in the developing polygon trough area, (b) MASW 2
 634 in the flat-centered polygon area, (c) MASW 3 in the low-centered polygon area, (d) MASW 4
 635 surrounded by thermokarst lakes, and (e) Roadside.

636 **5.5 Influence of civil infrastructure on permafrost**

637 In this section, we discuss the influence of civil infrastructures, including gravel roads
 638 and pile foundations, two of the most common civil infrastructures in Northern Alaska, based on
 639 seven MASW surveys. Comparison of V_s profiles of disturbed permafrost locations (Roadside

640 and NOAA 1) and relatively undisturbed permafrost locations nearby (NOAA 3 and MASW 1)
641 in Figure 4 demonstrates that the ALT is larger in disturbed permafrost due to higher surface
642 temperature. For NOAA 3 and MASW 1, the maximum V_s is similar (~900 m/s), but the high-
643 velocity zone is deeper (~4 m) in permafrost near civil infrastructure (NOAA 1) compared with
644 MASW 1 (~1 m). This discrepancy may be due to the disturbed gravel topsoil and also higher air
645 temperatures near civil infrastructure, causing diffusive heat transfer from a more absorptive
646 material and resulting in temperature profiles that differ from undisturbed permafrost locations.

647 The MASW testing location beside a gravel road is shown in Figure 8e (Roadside). In
648 cold regions, dry coarse-grained soil is often used to replace the foundation soil of roadbeds or
649 airport runways to prevent frost heave (Vinson et al., 1996). The gravel fill reduces the road's
650 frost heave and thaw settlement by providing better drainage capability but affects the moisture
651 regime near the gravel road. As shown in Figure 8, high-centered polygons developed near the
652 gravel road, with surface water accumulation next to the road embankment.

653 Ice-rich permafrost zones can be identified beneath the polygon landscape in the V_s
654 profiles shown in Figures 4 and 8. The depth of the ice-rich permafrost zone along the roadside
655 (Figure 3e) is shallower than the nearby tundra location at NOAA 3 (Figure 3g), suggesting the
656 influence of the gravel road. Along the roadside, the ice-rich permafrost zone (~4 m thickness) is
657 thicker than MASW 1. Different moisture migrations beside the gravel road may cause these
658 differences. In addition to unfrozen water migration as the dominant mode of moisture
659 movement, vapor flux also contributes to frost heaving (Currie, 1983; Farouki, 1981; Smith &
660 Burn, 1987; Teng et al., 2020). Gaseous water (vapor) migrates from the warm and humid side of
661 the soil layer to the cold and dry layer below the closed and impermeable ground surface in
662 coarse-grained soil and then condenses into ice, causing frost heaving (Guthrie et al., 2006; Niu
663 et al., 2017; Zhang et al., 2020). This phenomenon is known as the "pot effect" or "canopy
664 effect" (Bai et al., 2018). Generally, soil with an initial moisture content of less than 30% is more
665 prone to showing the "pot effect" (Bai et al., 2018).

666 Pile foundations are the most common building foundation type in Arctic Alaska to
667 overcome differential settlement. Figures 4f and 4g display the 2D V_s profiles for MASW
668 surveys under the NOAA building (NOAA 1), and ~80 meters from the building in the tundra
669 (NOAA 3), respectively. As shown in Figure 3, NOAA 1 shows a similar low-high-low V_s trend
670 to NOAA 3 (and also MASW 1-4). At depths of 0-2 m, shear wave velocities are slightly
671 different for NOAA 1 and NOAA 3 due to the topsoil of NOAA 1 being gravel, while NOAA 3
672 is tundra permafrost. At 2-8 m depths, NOAA 3 presents an ice-rich permafrost zone, while
673 NOAA 1 has much smaller V_s in this depth range, indicating softer soil. In addition, in NOAA 1,
674 we observed a ~150 m/s decrease in V_s for the ice-rich zone compared to the ice-rich zone at
675 NOAA 3 (farther into the tundra). This lower V_s in the ice-rich zone near the building suggests
676 that the pile foundation impacts the soil properties in the surrounding area. Although there is
677 lower V_s in the ice-rich zone near the building, the ice-rich zone near the building is more
678 laterally uniform than the ice-rich zone further in the tundra. Because the building had been
679 present in the area for many years, it could have contributed to the thawing and freezing of the
680 surrounding ground, leading to a more uniform distribution of ice-rich soil after years of thermal
681 diffusion of heat from the building. The substantial differences observed at these sites highlight
682 the need to consider the long-term effects of anthropogenic activities on the geological and
683 geotechnical properties of the ground.

684

685 5.6 Applications in quantifying engineering properties and designing infrastructure on 686 permafrost

687 Investigating the long-term effect of civil infrastructure on permafrost's stiffness could
688 help improve the engineering design of structures' foundations on permafrost. Permafrost's
689 parameters, such as V_{S30} and E , are affected by soil types (Coduto, 1999), soil temperature (Ji et
690 al., 2023), and soil's ice content (Fisher et al., 2020). Changes in these soil properties show
691 possible changes in soil types, thermal conditions, and cryostructure. For instance, the stability of
692 the subgrade in permafrost regions, as noted by Anhua (2014), is closely linked to the ice content
693 in the permafrost beneath roadways. Here, we quantitatively analyze V_s profiles at NOAA 1 and
694 NOAA 3 locations. Based on the MASW results, V_{S30} for locations NOAA 1 and NOAA 3 are
695 equal to 744.2 m/s and 799.5 m/s, respectively. This reduction can affect the soil's ability to carry
696 loads (as the soil at NOAA 1 is less stiff than the NOAA 3 location), leading to greater
697 settlement or deformation under structural loads. Assuming a $V_p/V_s = 1.6$ for the site's
698 permafrost layer based on (Ji et al., 2023), and γ and g equal to 19.62 kN/m³ and 9.81 m/s²,
699 respectively, equations 1-3 result in an elastic modulus of 261.07 MPa at NOAA 1 location and
700 301.31 MPa at NOAA 3 location. This indicates a 13.35% reduction in elastic modulus
701 accompanied by an equivalent increase in settlement values, as delineated by equation 4. While
702 our findings offer useful insights for designing and maintaining infrastructure in polar regions,
703 extending these findings to other permafrost settings should be approached with caution,
704 considering local variations in soil composition, temperature trends, and permafrost degradation.

705

706 6 Conclusions

707 This study uses 1D and 2D V_s profiles from MASW along with temperature
708 measurement, ERT, and permafrost sampling to reveal various permafrost features in Utqiagvik,
709 Alaska. V_s profiles, combined with electrical resistivity models and temperature measurements,
710 can qualitatively characterize active layer, ice-rich permafrost, and cryopeg in permafrost layer,
711 but cannot identify small-scale cryostructures such as ice lenses. V_s in active layer ranges from
712 240 to 370 m/s (silty peat to silt), while V_s in permafrost layer ranges from 450 to 1700 m/s (silt
713 to slightly sandy silt) in August 2022. V_s profiles demonstrate a consistent vertical low-high-low
714 velocity trend in permafrost. Ice content, ice layers, and ice-wedge influence shear wave
715 velocities, with higher V_s indicating higher ice content. Low V_s permafrost zones may exist
716 across the tundra near Elson Lagoon and east of Utqiagvik. The V_s variation in ice-rich
717 permafrost correlates with ground temperature variation at 0-15 m depths at the study region.
718 This correlation indicates that ice-rich permafrost with higher V_s values demonstrates lower
719 temperatures than active layer and ice-poor permafrost. By using ERT, multiple layers can be
720 identified at shallow depths: active layer (200-300 Ω m), cryopeg (10-20 Ω m), and ice-rich
721 permafrost (100-600 Ω m). The presence of ice becomes evident through the analysis of V_s and
722 ERT profiles. To strengthen our conclusions, we validate geophysical results with stratigraphy
723 and salinity analyses from permafrost cores. Integrating geophysical, temperature, and core
724 sampling methods offers a reliable approach to evaluating and understanding permafrost spatial
725 variability.

726 Civil infrastructure can impact permafrost, resulting in a higher active layer thickness and
727 lower V_s . The influence of gravel road and pile foundation on permafrost degradation varies.
728 Thicker ice-rich permafrost layers at shallower depths, surface water accumulation, and ice

729 polygon development are identified near the gravel road on permafrost. At the sites with building
730 and pile foundations, lower shear wave velocities are observed at depths shallower than 7 m
731 when compared to nearby undisturbed tundra. The active layer and permafrost are more laterally
732 homogeneous closer to the building compared to nearby undisturbed tundra, and a thinner high-
733 velocity zone exists closer to the building. The resulting V_s profile suggests weaker ground near
734 infrastructure, which should be accounted for by civil engineers.

735 **Acknowledgments**

736 This study is supported by the National Science Foundation under Grants CMMI-2034363,
737 CMMI-2034366, CMMI-2034380, and ICER-1927718. We express our gratitude to Geometrics
738 for providing us with the necessary equipment and software for our study. We also acknowledge
739 the support and facilities provided by UIC Science, LLC, the National Oceanic and Atmospheric
740 Administration (NOAA), and the Atmospheric Radiation Measurement Climate Research
741 Facility of the Department of Energy (DOE ARM). Dmitry Nicolsky acknowledges support from
742 the Tomsk State University Development Programme (Priority-2030). We thank Dr. Min Liew
743 for her valuable professional knowledge and advice, and Dr. Chris McComb for his assistance
744 with fieldwork. Our sincere thanks also go to Larry Irons, an IT support at Colorado School of
745 Mines, and Brian Passarella, equipment pool at Colorado School of Mines, for their invaluable
746 assistance throughout the study.

747

748 **Open Research**

- 749 • The seismic and ERT data used for geophysical data processing are available through the
750 Arctic Data Center Tourei et al., (2023) <https://doi:10.18739/A2V40K14Q>
- 751 • The seismic data were processed using the SeisImagerSW software (GeometricsTM,
752 Version 3.0.), with parameters described in Section 3.1.
- 753 • The ERT data were processed using Prosys II software (IRIS Instruments) and the
754 Res2Dinv software (Geotomo SoftwareTM, Version 3.59.), with parameters described in
755 Section 3.2.
- 756 • The temperature data are available through the Arctic Data Center Nicolsky & Wright,
757 (2023) <https://doi.org/10.18739/A2C53F305>
- 758 • The physical permafrost core samples in Figure 6 are registered and available through
759 SESAR with the International Geo Sample Number (IGSN) of IENNA0001
760 (<https://doi.org/10.58052/IENNA0001>), IENNA0002, IENNA0003, IENNA0007,
761 IENNA0008, IENNA0009, IENNA000A, IENNA000E, IENNA000F, IENNA000G,
762 IENNA000K, IENNA000L, IENNA000M, and IENNA000N.

763

764 **References**

765 Ajo-Franklin, J., Dou, S., Lindsey, N., Daley, T. M., Freifeld, B., Martin, E. R., Robertson, M.,
766 Ulrich, C., Wood, T., Eckblaw, I., & Wagner, A. (2017). Timelapse Surface Wave Monitoring of
767 Permafrost Thaw Using Distributed Acoustic Sensing and a Permanent Automated Seismic

- 768 Source. *SEG Technical Program Expanded Abstracts*, 5223–5227.
769 <https://doi.org/10.1190/SEGAM2017-17774027.1>
- 770 Alam, M. I., & Jaiswal, P. (2017). Near Surface Characterization Using VP/VS and Poisson's Ratio
771 from Seismic Refractions. *Journal of Environmental and Engineering Geophysics*, 22(2), 101–
772 109. <https://doi.org/10.2113/JEEG22.2.101>
- 773 AMAP, Arctic Climate Change Update (2021). Key Trends and Impacts. *Summary for Policy-*
774 *Makers, Arctic Monitoring and Assessment Programme (AMAP), Tromsø, Norway*, 16.
- 775 Anhua, X. U. (2014). Analysis of the sensitivity of highway diseases in permafrost regions to
776 ground temperatures and ice contents. *Journal of Glaciology & Geocryology*, 36(3), 622–625.
- 777 ASCE. (2017). ASCE/SEI 7-16. *Minimum Design Loads for Buildings and Other Structures*.
778 <https://doi.org/10.1061/9780784414248>
- 779 Bai, R., Lai, Y., Zhang, M., & Gao, J. (2018). Water-vapor-heat behavior in a freezing unsaturated
780 coarse-grained soil with a closed top. *Cold Regions Science and Technology*, 155, 120–126.
- 781 Bery, A. A., & Bery, A. A. (2013). High Resolution in Seismic Refraction Tomography for
782 Environmental Study. *International Journal of Geosciences*, 4(4), 792–796.
783 <https://doi.org/10.4236/IJG.2013.44073>
- 784 Biskaborn, B. K., Smith, S. L., Noetzli, J., Matthes, H., Vieira, G., Streletskiy, D. A., ... & Lantuit,
785 H. (2019). Permafrost is warming at a global scale. *Nature Communications*, 10(1), 264.
- 786 Bohlen, T. (2002). Parallel 3-D Viscoelastic Finite-Difference Seismic Modelling. *Computers &*
787 *Geosciences*, 28(8), 887–899.
- 788 Boiero, D., & Socco, L. V. (2011). The meaning of surface wave dispersion curves in weakly
789 laterally varying structures. *Near Surface Geophysics*, 9, 561–570. [https://doi.org/10.3997/1873-](https://doi.org/10.3997/1873-0604.2011042)
790 [0604.2011042](https://doi.org/10.3997/1873-0604.2011042)
- 791 Brothers, L. L., Herman, B. M., Hart, P. E., & Ruppel, C. D. (2016). Subsea ice-bearing permafrost
792 on the US Beaufort Margin: 1. Minimum seaward extent defined from multichannel seismic
793 reflection data. *Geochemistry, Geophysics, Geosystems*, 17(11), 4354–4365.
- 794 Brown, J. (1969) Ionic Concentration Gradients in Permafrost Barrow, Alaska, Cold Regions
795 Research and Engineering Laboratory, *Corps of Engineers, US Army, Hanover, New Hampshire*.
- 796 Carr, B. J., Hajnal, Z., & Prugger, A. (1998). Shear-wave studies in glacial till. 1273–1284.
797 *GEOPHYSICS*, 63(4), 1273–1284. <https://doi.org/10.1190/1.1444429>
- 798 Chen, J., Wu, Y., O'Connor, M., Cardenas, M. B., Schaefer, K., Michaelides, R., & Kling, G.
799 (2020). Active layer freeze-thaw and water storage dynamics in permafrost environments inferred
800 from InSAR. *Remote Sensing of Environment*, 248, 112007.
- 801 Coduto, D. P. (1999). *Geotechnical Engineering Principles and Practices*. Prentice-Hall, Inc.

- 802 Cox, B. R., Wood, C. M., & Hazirbaba, K. (2012). Frozen and unfrozen shear wave velocity
803 seismic site classification of Fairbanks, Alaska. *Journal of Cold Regions Engineering*, 26(3), 118-
804 145.
- 805 Currie, J. A. (1983). Gas diffusion through soil crumbs: the effects of wetting and swelling. *Journal*
806 *of Soil Science*, 34(2), 217-232.
- 807 Daily, W., Ramirez, A., Binley, A., & Labrecque, D. (2000). Electrical resistance tomography—
808 theory and practice. In *Near-surface Geophysics* (pp. 525-550). *Society of Exploration*
809 *Geophysicists*. <https://doi.org/10.1190/1.9781560801719.ch17>
- 810 Dafflon, B., Hubbard, S., Ulrich, C., Peterson, J., Wu, Y., Wainwright, H. and Kneafsey, T.J.
811 (2016) Geophysical estimation of shallow permafrost distribution and properties in an ice-wedge
812 polygon-dominated Arctic tundra region. *Geophysics* 81(1), WA247-WA263.
- 813 Dafflon, B., Oktem, R., Peterson, J., Ulrich, C., Tran, A.P., Romanovsky, V. and Hubbard, S.S.
814 (2017) Coincident aboveground and belowground autonomous monitoring to quantify
815 covariability in permafrost, soil, and vegetation properties in Arctic tundra. *Journal of Geophysical*
816 *Research: Biogeosciences* 122(6), 1321-1342.
- 817 Dal Moro, G., Pipan, M., Forte, E., & Finetti, I. (2003). Determination of rayleigh wave dispersion
818 curves for near surface applications in unconsolidated sediments. *SEG Technical Program*
819 *Expanded Abstracts*, 22(1), 1247–1250. <https://doi.org/10.1190/1.1817508>
- 820 Dou, S., & Ajo-Franklin, J. B. (2014). Full-wavefield inversion of surface waves for mapping
821 embedded low-velocity zones in permafrost. *Geophysics*, 79(6), EN107-EN124.
- 822 Dou, S., Ajo Franklin, J. B., & Dreger, D. S. (2012, December). Mapping Deep Low Velocity
823 Zones in Alaskan Arctic Coastal Permafrost using Seismic Surface Waves. In *AGU Fall Meeting*
824 *Abstracts* (Vol. 2012, pp. C22B-07).
- 825 Essien, U. E., Akankpo, A. O., & Igboekwe, M. U. (2014). Poisson's Ratio of Surface Soils and
826 Shallow Sediments Determined from Seismic Compressional and Shear Wave Velocities.
827 *International Journal of Geosciences*, 5(12), 1540–1546.
828 <https://doi.org/10.4236/IJG.2014.512125>
- 829 Etzelmüller, B., Guglielmin, M., Hauck, C., Hilbich, C., Hoelzle, M., Isaksen, K., ... & Ramos, M.
830 (2020). Twenty years of European mountain permafrost dynamics—the PACE legacy.
831 *Environmental Research Letters*, 15(10), 104070.
- 832 Evangelista, L., Santucci de Magistris, F. (2015). Some Limits in the Use of the MASW Technique
833 in Soils with Inclined Layers. *Geotech Geol Eng* 33, 701–711. [https://doi.org/10.1007/s10706-](https://doi.org/10.1007/s10706-015-9852-1)
834 [015-9852-1](https://doi.org/10.1007/s10706-015-9852-1)
- 835 Farouki, O. T. (1981). The thermal properties of soils in cold regions. *Cold Regions Science and*
836 *Technology*, 5(1), 67-75.

- 837 Farquharson, L. M., Romanovsky, V. E., Cable, W. L., Walker, D. A., Kokelj, S. V., & Nicolsky,
838 D. (2019). Climate change drives widespread and rapid thermokarst development in very cold
839 permafrost in the Canadian High Arctic. *Geophysical Research Letters*, *46*(12), 6681–6689.
- 840 Ferrians Jr, O. J. (1965). *Permafrost map of Alaska* (No. 445).
- 841 Fisher, D. A., Lacelle, D., & Pollard, W. (2020). A model of unfrozen water content and its
842 transport in icy permafrost soils: Effects on ground ice content and permafrost stability. *Permafrost
843 and Periglacial Processes*, *31*(1), 184-199.
- 844 Fortin, J., Guéguen, Y., & Schubnel, A. (2007). Effects of pore collapse and grain crushing on
845 ultrasonic velocities and Vp/Vs. *Journal of Geophysical Research: Solid Earth*, *112*(B8), 8207.
846 <https://doi.org/10.1029/2005JB004005>
- 847 Glazer, M., Dobiński, W., Marciniak, A., Majdański, M., & Błaszczuk, M. (2020). Spatial
848 distribution and controls of permafrost development in non-glacial Arctic catchment over the
849 Holocene, Fuglebekken, SW Spitsbergen. *Geomorphology*, *358*, 107128.
- 850 Guthrie, W. S., Hermansson, Å., & Woffinden, K. H. (2006). Saturation of granular base material
851 due to water vapor flow during freezing: laboratory experimentation and numerical modeling. In
852 *Current Practices in Cold Regions Engineering*(pp. 1-12).
- 853 Harris, C., & Cook, J. D. (1986). The detection of high altitude permafrost in Jotunheimen, Norway
854 using seismic refraction techniques: an assessment. *Arctic and Alpine Research*, *18*(1), 19-26.
- 855 Hayashi, K., & Suzuki, H. (2004). CMP cross-correlation analysis of multichannel surface-wave
856 data. In *Exploration Geophysics (Vol. 35, Issue 1)*.
- 857 Hazirbaba, K., Zhang, Y., & Hulsey, J. L. (2011). Evaluation of temperature and freeze–thaw
858 effects on excess pore pressure generation of fine-grained soils. *Soil dynamics and earthquake
859 engineering*, *31*(3), 372-384.
- 860 Herring, T., Lewkowicz, A. G., Hauck, C., Hilbich, C., Mollaret, C., Oldenborger, G. A., ... &
861 Scandroglio, R. (2023). Best practices for using electrical resistivity tomography to investigate
862 permafrost. *Permafrost and Periglacial Processes*, *34*(4), 494-512.
- 863 Hjort, J., Streletskiy, D., Doré, G., Wu, Q., Bjella, K., & Luoto, M. (2022). Impacts of permafrost
864 degradation on infrastructure. *Nature Reviews Earth & Environment*, *3*(1), 24-38.
- 865 Hubbard, S. S., Gangodagamage, C., Dafflon, B., Wainwright, H., Peterson, J., Gusmeroli, A., ...
866 & Ulrich, C. (2013). Quantifying and relating land-surface and subsurface variability in permafrost
867 environments using LiDAR and surface geophysical datasets. *Hydrogeology Journal*, *21*, 149–
868 169. <https://doi.org/10.1007/s10040-012-0939-y>
- 869 Ikeda, A. (2006). Combination of conventional geophysical methods for sounding the composition
870 of rock glaciers in the Swiss Alps. *Permafrost and Periglacial Processes*, *17*(1), 35-48.

- 871 IPCC. (2021). *Climate Change 2021: The Physical Science Basis, Contribution of Working Group*
872 *I to the Sixth Assessment Report of the Intergovernmental Panel on Climate Change*. Cambridge
873 University Press.
- 874 Iwahana, G., Cooper, Z. S., Carpenter, S. D., Deming, J. W., & Eicken, H. (2021). Intra-ice and
875 intra-sediment cryopeg brine occurrence in permafrost near Utqiagvik (Barrow). *Permafrost and*
876 *Periglacial Processes*, 32(3), 427-446.
- 877 Jafarov, E., Parsekian, A., Schaefer, K., Liu, L., Chen, A., Panda, S. K., & Zhang, T. (2018). Pre-
878 ABoVE: Active Layer Thickness and Soil Water Content, Barrow, Alaska, 2013. ORNL DAAC,
879 Oak Ridge, Tennessee, USA.
- 880 Ji, X., Xiao, M., Martin, E. R., & Zhu, T. (2023). Statistical Evaluation of Seismic Velocity Models
881 of Permafrost. *Earth ArXiv. Preprint*. <https://doi.org/10.31223/X55080>
- 882 Jorgenson, M. T., Yoshikawa, K., Kanevskiy, M., Shur, Y., Romanovsky, V., Marchenko, S., ...
883 & Jones, B. (2008, June). Permafrost characteristics of Alaska. In *Proceedings of the ninth*
884 *international conference on permafrost* (Vol. 3, pp. 121-122). University of Alaska.
- 885 Justice, J. H., & Zuba, C. (1986). Transition zone reflections and permafrost analysis. *Geophysics*,
886 51(5), 1075-1086.
- 887 Kanevskiy, M., Shur, Y., Jorgenson, M. T., Ping, C. L., Michaelson, G. J., Fortier, D., ... &
888 Tumskey, V. (2013). Ground ice in the upper permafrost of the Beaufort Sea coast of Alaska. *Cold*
889 *Regions Science and Technology*, 85, 56-70.
- 890 Kartoziia, A. (2019). Assessment of the ice wedge polygon current state by means of UAV imagery
891 analysis (Samoylov Island, the Lena Delta). *Remote Sensing*, 11(13), 1627.
892 <https://doi.org/10.3390/rs11131627>
- 893 Kerkering, J. (2008). Mapping past and future permafrost extent on the North Slope Borough,
894 Alaska.
- 895 Kneisel, C., Hauck, C., Fortier, R., & Moorman, B. (2008). Advances in geophysical methods for
896 permafrost investigations. *Permafrost and Periglacial Processes*, 19(2), 157-178.
897 <https://doi.org/10.1002/PPP.616>
- 898 Kohnen, H. (1974). The temperature dependence of seismic waves in ice. *Journal of Glaciology*,
899 13(67), 144-147.
- 900 Kurfurst, P. J. (1976). Ultrasonic wave measurements on frozen soils at permafrost temperatures.
901 *Canadian Journal of Earth Sciences*, 13(11), 1571-1576. <https://doi.org/10.1139/e76-163>
- 902 Langer, M., von Deimling, T. S., Westermann, S., Rolph, R., Rutte, R., Antonova, S., ... & Grosse,
903 G. (2023). Thawing permafrost poses environmental threat to thousands of sites with legacy
904 industrial contamination. *Nature Communications*, 14(1), 1721. [https://doi.org/10.1038/s41467-](https://doi.org/10.1038/s41467-023-37276-4)
905 [023-37276-4](https://doi.org/10.1038/s41467-023-37276-4)

- 906 Lantuit, H., Overduin, P. P., Couture, N., Wetterich, S., Aré, F., Atkinson, D., ... & Vasiliev, A.
907 (2012). The Arctic coastal dynamics database: A new classification scheme and statistics on Arctic
908 permafrost coastlines. *Estuaries and Coasts*, 35, 383-400.
- 909 Lara, M. J., McGuire, A. D., Euskirchen, E. S., Tweedie, C. E., Hinkel, K. M., Skurikhin, A. N.,
910 ... & Genet, H. (2015). Polygonal tundra geomorphological change in response to warming alters
911 future CO₂ and CH₄ flux on the Barrow Peninsula. *Global Change Biology*, 21(4), 1634-1651.
- 912 Letson, F., Barthelmie, R. J., Hu, W., Brown, L. D., & Pryor, S. C. (2019). Wind gust
913 quantification using seismic measurements. *Natural Hazards*, 99(1), 355–377.
914 <https://doi.org/10.1007/S11069-019-03744-8/FIGURES/11>
- 915 Liew, M., Ji, X., Xiao, M., Farquharson, L., Nicolsky, D., Romanovsky, V., ... & McComb, C.
916 (2022). Synthesis of physical processes of permafrost degradation and geophysical and
917 geomechanical properties of permafrost. *Cold Regions Science and Technology*, 198, 103522.
- 918 Liu, H., Maghoul, P., & Shalaby, A. (2021). Seismic physics-based characterization of permafrost
919 sites using surface waves. *Cryosphere Discussions*.
- 920 Loke, M. H., & Barker, R. D. (1996). Rapid least-squares inversion of apparent resistivity
921 pseudosections by a quasi-Newton method. *Geophysical Prospect*. 44, 131–152.
- 922 Majdański, M., Dobiński, W., Marciniak, A., Owoc, B., Glazer, M., Osuch, M., & Wawrzyniak,
923 T. (2022). Variations of permafrost under freezing and thawing conditions in the coastal catchment
924 Fuglebekken (Hornsund, Spitsbergen, Svalbard). *Permafrost and Periglacial Processes*, 33(3),
925 264–276. <https://doi.org/10.1002/ppp.2147>
- 926 Marciniak, A., Owoc, B., Grzyb, J., Glazer, M., Dobiński, W., & Majdański, M. (2018, April).
927 Seismic Tomography and MASW analysis of the results of Spitsbergen seismic experiment-case
928 study. In *EGU General Assembly Conference Abstracts* (p. 280).
- 929 Marciniak, A., Owoc, B., Wawrzyniak, T., Nawrot, A., Glazer, M., Osuch, M., ... & Majdański,
930 M. (2019, September). Near-Surface Geophysical Imaging of the Permafrost—Initial Result of
931 Two High Arctic Expeditions to Spitsbergen. In *25th European Meeting of Environmental and
932 Engineering Geophysics* (Vol. 2019, No. 1, pp. 1-5). European Association of Geoscientists &
933 Engineers.
- 934 Melvin, A. M., Larsen, P., Boehlert, B., Neumann, J. E., Chinowsky, P., Espinet, X., ... &
935 Marchenko, S. S. (2017). Climate change damages to Alaska public infrastructure and the
936 economics of proactive adaptation. *Proceedings of the National Academy of Sciences*, 114(2),
937 E122-E131.
- 938 Meyer, H., Schirrmeister, L., Andreev, A., Wagner, D., Hubberten, H.-W., Yoshikawa, K.,
939 Bobrov, A., Wetterich, S., Opel, T., Kandiano, E. and Brown, J. (2010) Lateglacial and Holocene
940 isotopic and environmental history of northern coastal Alaska - Results from a buried ice-wedge
941 system at Barrow. *Quaternary Science Reviews* 29(27-28), 3720-3735.

- 942 Miller, R. D., Laflen, D. R., Hunter, J. A., Burns, R. A., Good, R. L., Douma, M., ... & Carr, B. J.
943 (2000, August). Imaging permafrost with shallow P-and S-wave reflection. In *SEG International*
944 *Exposition and Annual Meeting* (pp. SEG-2000). SEG.
- 945 Mokhtar, T. A., Al-Yazjeen, T., Al-Shuhail, A. A., & Toksöz, M. N. (2015). Effect of near-surface
946 geological structures on the dispersion characteristics of Rayleigh waves. *Near Surface*
947 *Geophysics*, 13(5), 467-477.
- 948 Nakano, Y., Martin III, R. J., & Smith, M. (1972). Ultrasonic velocities of the dilatation and shear
949 waves in frozen soils. *Water Resources Research*, 8(4), 1024-1030.
950 <https://doi.org/10.1029/WR008i004p01024>
- 951 Nicolsky, D. J., Romanovsky, V. E., & Panteleev, G. G. (2009). Estimation of soil thermal
952 properties using in-situ temperature measurements in the active layer and permafrost. *Cold*
953 *Regions Science and Technology*, 55(1), 120-129.
- 954 Nicolsky, D. J., Romanovsky, V. E., Panda, S. K., Marchenko, S. S., & Muskett, R. R. (2017).
955 Applicability of the ecosystem type approach to model permafrost dynamics across the Alaska
956 North Slope. *Journal of Geophysical Research: Earth Surface*, 122(1), 50-75.
- 957 Nicolsky, D. J., & Wright, T. (2023). Understand and forecast long-term variations of in-situ
958 geophysical and geomechanical characteristics of degrading permafrost in the Arctic -
959 continuously observed ground temperatures, 2021-2022 .[Dataset]. Arctic Data Center.
960 <https://doi.org/10.18739/A2C53F305>
- 961 Nitzbon, J., Langer, M., Westermann, S., Martin, L., Aas, K. S., & Boike, J. (2019). Pathways of
962 ice-wedge degradation in polygonal tundra under different hydrological conditions. *The*
963 *Cryosphere*, 13(4), 1089-1123.
- 964 Niu, F., Li, A., Luo, J., Lin, Z., Yin, G., Liu, M., ... & Liu, H. (2017). Soil moisture, ground
965 temperatures, and deformation of a high-speed railway embankment in Northeast China. *Cold*
966 *Regions Science and Technology*, 133, 7-14.
- 967 O'Sullivan, J. B. (1966). Geochemistry of permafrost, Barrow, Alaska. In *Permafrost International*
968 *Conference* (pp. 30-37). Lafayette, Ind: National Academy of Sciences. Overduin, P. P.,
969 Westermann, S., Yoshikawa, K., Haberlau, T., Romanovsky, V., & Wetterich, S. (2012).
970 Geoelectric observations of the degradation of nearshore submarine permafrost at Barrow
971 (Alaskan Beaufort Sea). *J. Geophys. Res.*, 117, F02004. <https://doi.org/10.1029/2011JF002088>
- 972 Park, C. B. (2011). Imaging dispersion of MASW data - Full vs. Selective offset scheme. *Journal*
973 *of Environmental and Engineering Geophysics*, 16(1). <https://doi.org/10.2113/JEEG16.1.13>
- 974 Park, C. B., Miller, R. D., & Xia, J. (1999a). Multimodal Analysis of High Frequency Surface
975 Waves. In *Symposium on the Application of Geophysics to Engineering and Environmental*
976 *Problems 1999* (pp. 115–121). Environment and Engineering Geophysical Society.
977 <https://doi.org/doi:10.4133/1.2922596>

- 978 Park, C. B., Miller, R. D., & Xia, J. (1999b). Multichannel analysis of surface waves.
979 *GEOPHYSICS*, 64(3), 800–808. <https://doi.org/10.1190/1.1444590>
- 980 Park, C. B., Miller, R. D., Xia, J., & Survey, K. G. (1998). Imaging dispersion curves of surface
981 waves on multichannel record. *SEG Technical Program Expanded Abstracts*. Proceedings of the
982 National Academy of Sciences, 114(2), pp.E122-E131.
- 983 Picotti, S., Vuan, A., Carcione, J. M., Horgan, H. J., & Anandakrishnan, S. (2015). Anisotropy and
984 crystalline fabric of Whillans Ice Stream (West Antarctica) inferred from multicomponent seismic
985 data. *Journal of Geophysical Research: Solid Earth*, 120(6), 4237-4262.
- 986 Res2Dinv Manual (2006). Geoelectrical Imaging 2D and 3D. (Version 3.59.) [Software]. Geotomo
987 Software™.
- 988 Ramachandran, K., Bellefleur, G., Brent, T., Riedel, M., & Dallimore, S. (2011). Imaging
989 permafrost velocity structure using high resolution 3D seismic tomography. *Geophysics*, 76(5),
990 B187-B198.
- 991 Rantanen, M., Karpechko, A. Y., Lipponen, A., Nordling, K., Hyvärinen, O., Ruosteenoja, K.,
992 Vihma, T., & Laaksonen, A. (2022). The Arctic has warmed nearly four times faster than the globe
993 since 1979. *Communications Earth & Environment*, 3(1), 1-10.
- 994 Romanovsky, V. E., Drozdov, D. S., Oberman, N. G., Malkova, G. V., Kholodov, A. L.,
995 Marchenko, S. S., ... & Vasiliev, A. A. (2010). Thermal state of permafrost in Russia. *Permafrost
996 and Periglacial Processes*, 21(2), 136-155.
- 997 Rossi, M., Dal Cin, M., Picotti, S., Gei, D., Isaev, V.S., Pogorelov, A.V., Gorshkov, E.I.,
998 Sergeev, D.O., Kotov, P.I., Giorgi, M., Rainone, M.L. (2022) Active Layer and Permafrost
999 Investigations Using Geophysical and Geocryological Methods - A Case Study of the Khanovey
1000 Area, Near Vorkuta, in the NE European Russian Arctic. *Front. Earth Sci.* 10, 910078. doi:
1001 10.3389/feart.2022.910078
- 1002 Rossi, G., Accaino, F., Boaga, J., Petronio, L., Romeo, R., & Wheeler, W. (2018). Seismic survey
1003 on an open pingo system in Adventdalen Valley, Spitsbergen, Svalbard. *Near Surface Geophysics*,
1004 16(1), 89-103.
- 1005 Rocha dos Santos, G., Czarny, R., Roth, N., Zhu, T., Tourei, A., Martin, E. R., Ji, X., Liew, M.,
1006 Jensen, A. M., Nicolsky, D., & Xiao, M. (2022). Identification of Cryoseismic Events in Utqiagvik,
1007 Alaska Using Distributed Acoustic Sensing (DAS). *AGU Fall Meeting Abstracts, 2022*, NS45B-
1008 0326.
- 1009 Ryden, N., Park, C. B., Ulriksen, P., & Miller, R. D. (2004). Multimodal Approach to Seismic
1010 Pavement Testing. *Journal of Geotechnical and Geoenvironmental Engineering*, 130(6).
1011 [https://doi.org/10.1061/\(asce\)1090-0241\(2004\)130:6\(636\)](https://doi.org/10.1061/(asce)1090-0241(2004)130:6(636))
- 1012 Schrott, L., & Hoffmann, T. (2008). Refraction seismics. *Applied Geophysics in periglacial
1013 environments*, 57-79.

- 1014 Schwamborn, G. J., Dix, J. K., Bull, J. M., & Rachold, V. (2002). High-resolution seismic and
1015 ground penetrating radar–geophysical profiling of a thermokarst lake in the western Lena Delta,
1016 Northern Siberia. *Permafrost and Periglacial Processes*, *13*(4), 259-269.
- 1017 Scott, J. H., & Markiewicz, R. D. (1990). Dips and Chips—PC Programs for Analyzing Seismic
1018 Refraction Data. In *Symposium on the Application of Geophysics to Engineering and*
1019 *Environmental Problems 1990* (pp. 175-200). Society of Exploration Geophysicists.
- 1020 SeisImager/SWTM Manual (2009). SeisImager/SWTM. (Version 3.0.) [Software]. Geometrics Inc.
- 1021 Shiklomanov, N. I., Streletskiy, D. A., Nelson, F. E., Hollister, R. D., Romanovsky, V. E.,
1022 Tweedie, C. E., ... & Brown, J. (2010). Decadal variations of active-layer thickness in moisture-
1023 controlled landscapes, Barrow, Alaska. *Journal of Geophysical Research: Biogeosciences*,
1024 *115*(G4).
- 1025 Smith, M. W., & Burn, C. R. (1987). Outward flux of vapour from frozen soils at Mayo, Yukon,
1026 Canada: results and interpretation. *Cold Regions Science and Technology*, *13*(2), 143-152.
- 1027 Smith, S. L., O'Neill, H. B., Isaksen, K., Noetzli, J., & Romanovsky, V. E. (2022). The changing
1028 thermal state of permafrost. *Nature Reviews Earth & Environment*, *3*(1), 10–23.
1029 <https://doi.org/10.1038/s43017-021-00240-1>
- 1030 Socco, L. V., & Strobbia, C. (2004). Surface-wave method for near-surface characterization: A
1031 tutorial. *Near surface geophysics*, *2*(4), 165-185.
- 1032 Streletskiy, D. A., Anisimov, O., & Vasiliev, A. (2015). Permafrost degradation. In *Snow and ice-*
1033 *related hazards, risks, and disasters* (pp. 303-344). Academic Press.
- 1034 Streletskiy, D. A., Shiklomanov, N. I., & Nelson, F. E. (2012). Permafrost, infrastructure, and
1035 climate change: a GIS-based landscape approach to geotechnical modeling. *Arctic, Antarctic, and*
1036 *Alpine Research*, *44*(3), 368-380.
- 1037 Taylor, O. D. S., Abdollahi, M., & Vahedifard, F. (2022). Statistical distributions of wave
1038 velocities and elastic moduli in near-surface unsaturated soils. *Soil Dynamics and Earthquake*
1039 *Engineering*, *157*, 107247.
- 1040 Teng, J., Liu, J., Zhang, S., & Sheng, D. (2020). Modelling frost heave in unsaturated coarse-
1041 grained soils. *Acta Geotechnica*, *15*, 3307-3320.
- 1042 Terzaghi, K., Peck, R. B., & Mesri, G. (1996). *Soil mechanics in engineering practice*. John Wiley
1043 & sons.
- 1044 Thoman, R., & Walsh, J. E. (2019). Alaska's changing environment: Documenting Alaska's
1045 physical and biological changes through observations. *International Arctic Research Center*,
1046 *University of Alaska Fairbanks*.
- 1047 Tourei, A., Ji, X., Rocha dos Santos, G., Czarny, R., Rybakov, S., Wang, Z., Hallissey, M., Martin,
1048 E. R., Xiao M., Zhu, T., Nicolsky, D., Jensen, A., & McComb, C., (2023). Seismic and Electrical

- 1049 Resistivity Datasets for Characterizing Permafrost in Alaska (August 2023). [Dataset]. Arctic Data
1050 Center. <https://doi:10.18739/A2V40K14Q>
- 1051 Tourei, A., Martin, E. R., Rocha dos Santos, G., Czarny, R., Roth, N., Zhu, T., Ji, X., Liew, M.,
1052 Jensen, A. M., Nicolsky, D., & Xiao, M. (2022). Exploration and Quality Control of Large-scale
1053 Distributed Acoustic Sensing Data to Study Permafrost Degradation in Arctic Alaska. *AGU Fall*
1054 *Meeting Abstracts, 2022*, NS22B-0291.
- 1055 Van Everdingen, R. O. (Ed.). (1998). *Multi-language glossary of permafrost and related ground-*
1056 *ice terms in Chinese, English, French, German, Icelandic, Italian, Norwegian, polish, Romanian,*
1057 *Russian, Spanish, and Swedish*. International Permafrost Association, Terminology Working
1058 Group.
- 1059 Vinson, T. S., Rooney, J. W., & Haas, W. H. (Eds.). (1996). *Roads and airfields in cold regions:*
1060 *a state of the practice report*. ASCE Publications.
- 1061 Wagner, F. M., Mollaret, C., Günther, T., Kemna, A., & Hauck, C. (2019). Quantitative imaging
1062 of water, ice and air in permafrost systems through petrophysical joint inversion of seismic
1063 refraction and electrical resistivity data. *Geophysical Journal International*, 219(3), 1866-1875.
- 1064 Walker, D. A., Raynolds, M. K., Kanevskiy, M. Z., Shur, Y. S., Romanovsky, V. E., Jones, B. M.,
1065 ... & Peirce, J. L. (2022). Cumulative impacts of a gravel road and climate change in an ice-wedge-
1066 polygon landscape, Prudhoe Bay, Alaska. *Arctic Science*, 8(4), 1040-1066.
- 1067 Xia, J., Miller, R. D., & Park, C. B. (1999). Configuration of Near-Surface Shear-Wave Velocity
1068 by Inverting Surface Wave. In *Symposium on the Application of Geophysics to Engineering and*
1069 *Environmental Problems 1999* (pp. 95–104). Environment and Engineering Geophysical Society.
1070 <https://doi.org/doi:10.4133/1.2922698>
- 1071 Yilmaz, O. (1987). Seismic data processing. *Investigation in geophysics*, 2, 526.
- 1072 Yoshikawa, K., Romanovsky, V., Duxbury, N., Brown, J., & Tsapin, A. (2004). The use of
1073 geophysical methods to discriminate between brine layers and freshwater taliks in permafrost
1074 regions. *J. Glaciol. Geocryology* 26, 301–309.
- 1075 You, Y., Wang, J., Wu, Q., Yu, Q., Pan, X., Wang, X., & Guo, L. (2017). Causes of pile foundation
1076 failure in permafrost regions: The case study of a dry bridge of the Qinghai-Tibet Railway.
1077 *Engineering Geology*, 230, 95-103.
- 1078 Zhang, Y., Wen, A., Zhao, W., Liang, X., Li, P., & Černý, R. (2020). Influence of Compaction
1079 Level on the Water-Heat-Vapor Characteristics of Unsaturated Coarse-Grained Fillings Exposed
1080 to Freezing and Thawing. *Advances in Civil Engineering*, 2020, 1-10.